Preprint
LLNL-BOOK-410095

Dislocations and Plasticity in bcc Transition Metals at High Pressure

Lin H. Yang, Meijie Tang and John A. Moriarty

This article has been accepted for publication in Dislocations in Solids, Volume 16

January 30, 2009

Approved for public release; further dissemination unlimited

DISCLAIMER

This document was prepared as an account of work sponsored by an agency of the United States government. Neither the United States government nor Lawrence Livermore National Security, LLC, nor any of their employees makes any warranty, expressed or implied, or assumes any legal liability or responsibility for the accuracy, completeness, or usefulness of any information, apparatus, product, or process disclosed, or represents that its use would not infringe privately owned rights. Reference herein to any specific commercial product, process, or service by trade name, trademark, manufacturer, or otherwise does not necessarily constitute or imply its endorsement, recommendation, or favoring by the United States government or Lawrence Livermore National Security, LLC. The views and opinions of authors expressed herein do not necessarily state or reflect those of the United States government or Lawrence Livermore National Security, LLC, and shall not be used for advertising or product endorsement purposes.

Dislocations and Plasticity in bcc Transition Metals at High Pressure

Lin H. Yang, Meijie Tang and John A. Moriarty
Lawrence Livermore National Laboratory
Livermore, California 94551-0808

Abstract

Using first-principles electronic structure calculations, quantum-based atomistic simulations and atomistically informed dislocation dynamics (DD) simulations, we have studied individual dislocation behavior and the multiscale modeling of single-crystal plasticity in the prototype bcc transition metals Ta, Mo and V under both ambient and high pressure conditions. The primary focus in this work is on the pressure-dependent structure, mobility and interaction of $a/2<111>$ screw dislocations, which dominate the plastic deformation properties of these materials. At the electronic scale, first-principles calculations of elasticity, ideal strength and generalized stacking fault energy surfaces have been used to validate quantum-based multi-ion interatomic potentials. At the atomistic scale, these potentials have been used in flexible Green's function boundary condition simulations to study the core structure, Peierls stress τ_P, thermally activated kink-pair formation and mobility below τ_P, and phonon-drag mobility above τ_P. These results have then been distilled into analytic velocity laws and used directly in predictive microscale DD simulations of flow stress and resolved yield stress over wide ranges of pressure, temperature and strain rate.

Contents

1. Introduction

2. Computational Approach
2.1 First-principles electronic structure methods
2.2 Quantum-based interatomic potentials
2.3 Green's function atomistic simulation
2.4 Dislocation dynamics simulation

3. Salient High-Pressure Mechanical Properties of bcc Transition Metals
3.1 Bulk and shear elastic moduli
3.2 Ideal shear strength
3.3 Generalized stacking-fault (γ) energy surfaces

4. *a*/2 <111> Screw Dislocation Properties at High Pressure
4.1 Equilibrium core structure and energy
4.2 Low shear stress limit: kink-pair formation
4.3 High shear stress limit: Peierls stress
4.4 Activation enthalpy
4.5 Dislocation mobility near and above the Peierls stress

5. Multiscale Modeling of Single-Crystal Plasticity
5.1 Analytic representations of dislocation velocity
5.2 Temperature- and pressure-dependent plastic flow

6. Summary and Conclusions

1. Introduction

The intriguing possibility of modeling across length scales all the way from the atomic level to the continuum level to achieve a physics-based multiscale description of mechanical properties such as plasticity and strength has attracted widespread research interest in the last decade [1-8]. To be sure, the predictive multiscale materials modeling of plasticity and strength requires an in depth theoretical understanding and quantum-based calculation of fundamental dislocation and other defect processes at the atomic length scale [9-19] as essential input into higher-length-scale simulations such as 3D dislocation dynamics (DD) of single-crystal plasticity at the microscale [20-31]. Especially important is the accurate atomistic modeling of the structure, motion and interaction of individual dislocations, as well as the accurate modeling of the relevant aspects of elasticity, including elastic moduli and the limits of elastic stability. To accomplish this task fully, one not only needs to understand the underlying *qualitative mechanisms* that control plastic deformation, but one also needs to be able to calculate the *quantitative parameters* that will allow a predictive description of plasticity and strength properties in real materials under various conditions. The latter is particularly important in regimes where experimental data are scarce or nonexistent such as under the extreme conditions of pressure, temperature, strain and strain rate of current interest to many modern applications. Especially interesting in this regard is the regime of high pressure, a regime in which dislocation-driven plasticity has been heretofore largely unexplored from a fundamental perspective. The objective of the present paper is to help fill that void. Specifically, we elaborate here a predictive multiscale description of dislocation behavior and single-crystal plasticity in bcc transition metals over a wide range of pressures, ranging from ambient all the way up to many hundreds of gigapascal (GPa). In this process we build upon and greatly extend the multiscale dislocation work on these materials previously reported by the present authors and their collaborators [13,14,16,19].

In recent years since the mid 1990s, there has been considerable renewed interest in understanding dislocation behavior and plastic deformation in bcc metals [1-6,9-19,21-23,27-32], where even at ambient pressure much remains unknown at the atomistic level about the fundamental mechanisms and quantitative parameters of dislocation motion. The numerous studies published on these materials over the years, especially the pioneering papers by Vitek and Duesbery [32-36], have identified many of the basic characteristics of dislocation behavior in bcc metals and have laid the groundwork for our investigations. In particular, at ambient pressure the low-temperature and high-strain-rate plastic behaviors of these metals are controlled by the intrinsic core properties of screw dislocations with Burgers vector $\boldsymbol{b} = a/2<111>$, where a is the bcc lattice constant. Unlike the highly mobile edge dislocations

in bcc metals, the motion of the $a/2<111>$ screw dislocations is severely restricted by the non-planar atomic structure of its core, resulting in low intrinsic mobility, the formation of thermally activated kinks on the dislocation line at finite temperature, and a temperature-dependent yield stress. Since these unique qualitative characteristics are closely tied to the bcc structure itself, we expect them to remain in effect at high pressure as well. We will, therefore, concentrate here on pressure-dependent $a/2<111>$ screw-dislocation behavior in the bcc lattice and the single-crystal plasticity that it drives.

At the same time, an important general consideration is the identification and separation of purely *generic* behavior representative of bcc metals as a whole from *materials-specific* behavior representative of chemical differences and environmental factors such as high pressure. The historical perspective has been to assume that bcc dislocation behavior and plasticity is highly generic in character. The expectation of possible materials-specific behavior under high pressure, however, underscores the importance of chemical bonding, in addition to crystal symmetry, in elaborating dislocation and strength properties. In bcc metals, chemical bonding ranges from non-directional, nearly-free-electron *sp* bonding in the alkali metals (e.g., Na, K) to directional *d*-electron bonding in transition metals (e.g., Ta, Mo, Fe). The latter also depends strongly on pressure-sensitive *d*-electron occupation, which can vary significantly within nonmagnetic group-VB (e.g., V, Ta) and group-VIB (e.g., Mo, W) elements, as well as between these elements and magnetic group-VIII elements (e.g., Fe). Here we will focus on a small subset of the nonmagnetic materials as prototypes, namely V, Ta and Mo, and examine in detail how their mechanical properties vary under the influence of high pressure. These materials have different ranges of bcc stability, as well as different high-pressure elastic behavior. While Ta is predicted to remain stable in the bcc phase up to at least 1000 GPa [37], Mo and V undergo high-pressure phase transitions, which are predicted above 500 GPa in the case of Mo [38,39] and observed near 69 GPa in the case of V [40]. The latter transition has also been confirmed theoretically [41]. The phase transitions in Mo and V are closely coupled, respectively, with the elastic softening of the C' and the C_{44} shear modulus in the compressed bcc lattice prior to the transitions.

Large-scale computer simulation is the enabling tool of multiscale modeling and is at the heart of the present investigation. This approach is not entirely unique, however, and involves a number of important strategic, physical and computational issues and choices. Here we have adopted an information passing strategy to the multiscale modeling of single-crystal plasticity across three overlapping length scales: electronic, atomic and micro- or mesoscopic. Crystal elastic moduli and the basic core properties of dislocations at the

electronic length scale are govern by the laws of quantum mechanics, which can be implemented from first principles via modern density functional theory (DFT) [42-44] in both full-potential (FP) and pseudopotential (PP) electronic-structure methods [37-39,44-47]. We use DFT electronic-structure calculations to establish the pressure dependence of certain key mechanical properties, including the shear elastic moduli, the ideal shear strength and the generalized stacking-fault (γ) energy surface. On the other hand, one can study the structure, motion and interaction of individual dislocations in much greater detail at the atomic length scale through static and dynamic atomistic simulations, using suitable quantum-based *interatomic potentials* that encode the necessary quantum information. For transition metals, DFT-based generalized pseudopotential theory (GPT) [49] provides a rigorous approach to obtain the required potentials. In our present multiscale strategy, we perform additional DFT electronic-structure calculations to establish a large data base of fundamental pressure-dependent properties of the zero-temperature bcc phase of each metal of interest, and then use this data base to constrain and validate simplified *model* GPT or MGPT multi-ion potentials [50], which in turn permit efficient atomistic simulations with full quantum realism. In particular, the MGPT potentials encode the fundamental directional bonding of central transition metals through explicit three- and four-ion angular-dependent terms, and can be used to make predictive calculations of high-pressure dislocation properties.

Atomistic simulations of point and extended defects are performed on a specified finite collection of atoms contained within a chosen computational cell of variable shape and size to which specific boundary conditions and other constraints such as temperature, stress and strain rate are applied. Both molecular statics (MS) techniques, which seek to minimize the total energy of the system at zero-temperature, and finite-temperature molecular dynamics (MD) techniques can be used. The simulation of individual dislocations requires special treatment due to the long-ranged ($\sim 1/r$) elastic field associated with them. Traditionally, fixed boundary conditions have been most often used in such dislocation simulations, where exterior atoms are frozen at their bulk lattice positions and distant atomic positions in the computational cell are established by the conditions of linear anisotropic elasticity. This requires very large simulation cells in practice, but this method is always problematic with respect to force build-up between fixed and relaxed atomic regions. An elegant and practical solution to the latter problem is to use so-called flexible boundary conditions. In particular, Rao *et al.* [51,52] have developed an advanced Green's-function version of such conditions for both 2D and 3D dislocation simulations, denoted as Green's function boundary conditions (GFBC). In this method, a buffer layer is introduced between the fixed outer and inner relaxed atomistic regions of the simulation cell, allowing one to dynamically update the

boundary conditions of the simulation, while dramatically reducing the size of the atomistic region. Using the GFBC approach, we subsequently developed a specialized Green's function atomistic simulation method to implement multi-ion MGPT potentials and calculate the pressure-dependent properties of $a/2<111>$ screw dislocations through MS and MD simulations [13]. These properties include the core structure and energy, the kink pair formation energy, and the Peierls stress τ_P, as well as the full activation enthalpy below τ_P and the phonon drag mobility above τ_P needed to describe dislocation motion in DD microscale simulations.

At the microscale, dislocation dynamics simulations implement the equations of continuum elasticity theory to track the motion and interaction of individual dislocations under an applied stress, leading to the development of a dislocation microstructure and single-crystal plastic deformation. In our multiscale modeling strategy for bcc transition metals, the primary atomistic input supplied to the DD simulations is the dislocation mobility of individual $a/2<111>$ screw dislocations. For a given material, this input takes the form of an activation enthalpy versus shear stress curve and phonon drag coefficients calculated for each pressure under consideration. Here full activation enthalpy curves have been calculated at selected pressures in Ta, Mo and V, and phonon drag has been studied as a function of pressure and temperature in the case of Ta. These results have been fitted and modeled in suitable analytic forms to interface smoothly with the DD simulation codes. Detailed DD simulations have then been carried out in Ta and Mo as a function of pressure, temperature and strain rate. Our DD simulations have been performed in part with the pioneering lattice-based serial code developed for bcc metals [21,22] but even more extensively with the general node-based parallel ParaDiS code recently developed at the Lawrence Livermore National Laboratory [27-30].

2. Computational Approach

We begin by introducing and briefly discussing the specific computational methods we have used in the present work to implement our multiscale modeling strategy for bcc transition metals.

2.1 First-principles electronic structure methods

The first-principles DFT electronic-structure results used below to constrain and validate MGPT potentials and to calculate basic high-pressure properties have been obtained with either the full-potential linear muffin-tin orbital (FP-LMTO) method [37-39,44,45,47] or the plane-wave pseudopotential (PP) method [44-46,48]. The FP-LMTO method was used previously to study basic structural and mechanical properties in Ta to 1000 GPa (10 Mbar) [37], as well as in Mo [38,39] and in V [47] to 600 GPa (6 Mbar). These data are used here in establishing the zero-temperature equation of state (cold EOS or pressure versus volume curve) and the high-pressure shear elastic moduli. The FP-LMTO and PP methods were also used previously to study vacancy formation in bcc metals, including Ta, Mo and V [45]. Together with the cold EOS and shear elastic moduli, FP-LMTO and PP data on the vacancy formation energy are used to constrain the MGPT potentials. To help further validate the potentials at high pressure for the present dislocations studies, entirely new PP results have been obtained here on the ideal shear strength and high-symmetry features of the {110} and {211} γ surfaces to 400 GPa in Ta and Mo and to 140 GPa in V.

The FP-LMTO and PP methods have been implemented from first-principles within the DFT and require only the atomic number and an assumed functional form for the exchange and correlation energy of the electrons as input. Historically, the latter functional has been treated both within the standard local-density approximation (LDA) [43,44] and the more modern generalized gradient approximation (GGA) [44]. In general, the GGA is believed to provide the more accurate treatment for central transition metals and has been used in all of the FP-LMTO and PP results discussed here. In both the FP-LMTO and PP approaches, the electron charge density and potential are allowed to have any geometrical shape and are calculated self-consistently. In the FP-LMTO method all electrons are treated, including tightly-bound inner-core, loosely bound outer-core and itinerate valence electrons, to ensure that their rapidly changing character under pressure is fully accommodated. One incorporates non-sphericity to the charge density and potential by representing the crystal with non-overlapping spheres (of a variable, optimum size) surrounding each atomic site and a general shaped interstitial region between the spheres. Inside the spheres, the wave functions are represented

as Bloch sums of linear muffin-tin orbitals and are expanded by means of structure constants. The kinetic energy is not restricted to be zero in the interstitial region and the wave function expansion contains Hankel or Neumann functions (depending on sign of the kinetic energy) together with Bessel functions. Also in the FP-LMTO method, all relativistic terms, including the spin-orbit coupling, can included in the Hamiltonian as necessary, and this has been done in the results used here in the case of Ta. The metals V and Mo have been treated in a semi-relativistic fashion without the spin-orbit coupling.

In the PP method applied to transition metals one normally treats only the valence *s*, *p* and *d* electrons, which total five per atom in V and Ta and six per atom in Mo. Here special pseudopotentials in the Troullier-Martins form [48] have been constructed from scalar-relativistic atomic calculations to be accurate in the pressure range below 400 GPa. An important advantage of the PP method is that it provides accurate forces so that fully relaxed atomic configurations can be considered. We have used this capability here to obtain accurate relaxed {110} and {211} γ surfaces for Ta, Mo and V. It is also possible to use relaxed PP configurations to perform validating FP-LMTO calculations on relaxed defects and γ surfaces, as was done previously at ambient pressure [13,45].

2.2 Quantum-based interatomic potentials

Within DFT quantum mechanics, first-principles generalized pseudopotential theory (GPT) provides a fundamental basis for *ab initio* interatomic potentials in metals and alloys. In the GPT applied to transition metals [49], a mixed basis of plane waves and localized *d*-state orbitals is used to self-consistently expand the electron density and total energy of the system in terms of weak *sp* pseudopotential, *d-d* tight-binding, and *sp-d* hybridization matrix elements, which in turn are all directly calculable from first principles. For a bulk transition metal, one obtains the real-space total-energy functional

$$E_{tot}(R_1 \ldots R_N) = NE_{vol}(\Omega) + \frac{1}{2}\sum_{i,j}{}' v_2(ij;\Omega) + \frac{1}{6}\sum_{i,j,k}{}' v_3(ijk;\Omega) + \frac{1}{24}\sum_{i,j,k,l}{}' v_4(ijkl;\Omega) \qquad (1)$$

The leading volume term in this expansion, E_{vol}, as well as the two-, three-, and four-ion interatomic potentials, v_2, v_3 and v_4, are volume dependent, *but structure independent* quantities and thus *transferable* to arbitrary bulk ion configurations. The angular-force multi-ion potentials v_3 and v_4 reflect directional-bonding contributions from partially-filled *d* bands and are important for mid-period transition metals. In the full GPT, however, these potentials

are multi-dimensional functions, so that v_3 and v_4 cannot be readily tabulated for application purposes. This has led to the development of a simplified *model* GPT or MGPT, which achieves short-ranged, analytic potential forms that can be applied to large-scale atomistic simulations [50].

The MGPT is derived from the GPT through a series of systematic approximations applicable to central transition metals. Canonical *d* bands are introduced to express the *d*-state components of v_2 and the multi-ion potentials v_3 and v_4 analytically in terms of a single radial function and three universal angular functions that depend only on *d* symmetry and apply to all transition metals and all volumes. To compensate for the approximations introduced into the MGPT, the *d*-state potential coefficients in v_2, v_3 and v_4 together with E_{vol} are constrained by fundamental theoretical and/or experimental data. In our current preferred scheme for bcc metals, we fit a combination of first-principles DFT calculations and experimental data on the cold equation of state, shear elastic moduli, unrelaxed vacancy formation energy and Debye temperature over a prescribed volume or pressure range. Advanced generation MGPT potentials have been so obtained in Ta to 1000 GPa [13,14], in Mo to 400 GPa [16,53] and in V to 230 GPa [53]. Representative results for these three metals are displayed in Fig. 1 at their respective equilibrium volumes.

2.3 Green's function atomistic simulation

Previously, the flexible Green's function boundary condition (GFBC) method of Rao *et al.* [51,52] for dynamically updating the boundary conditions used in atomistic simulations was implemented for MGPT potentials and applied to study Ta dislocation properties at ambient

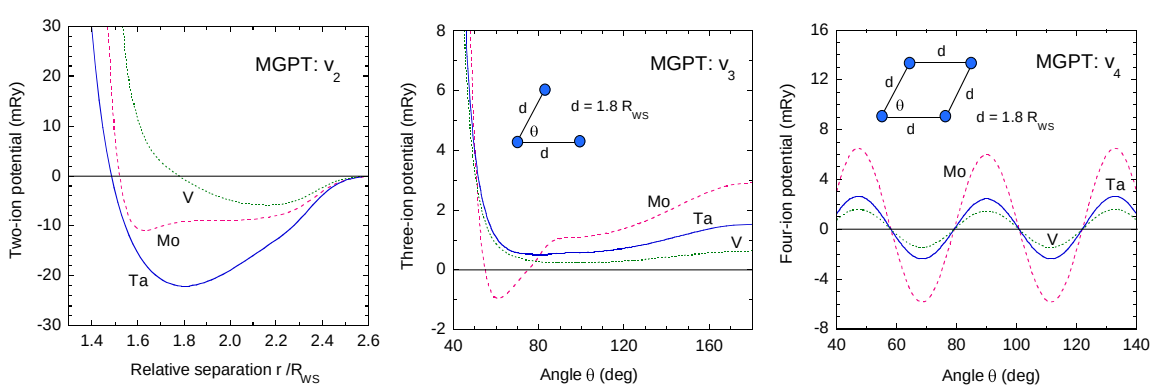

Figure 1. Present advanced generation MGPT multi-ion potentials v_2, v_3 and v_4 for Ta, Mo and V calculated at their respective equilibrium volumes.

pressure [13]. This same approach has been used here to study $a/2<111>$ dislocation core structure and mobility at high pressure in Ta, Mo and V. The GFBC approach extends the 2D lattice Green's function boundary relaxation method originated by Sinclair *et al.* [57] for treating rigid, straight dislocations to 3D simulations, including kink and kink-pair formation. The boundary conditions for 2D and 3D defect simulations cells are evaluated using line [58] and point [59] force distributions, respectively. In the flexible GFBC method, the simulation cell is divided into three regions, denoted as atomistic, Green's function (GF), and continuum. In the outer continuum region, the atomic positions are initially determined according to the anisotropic elastic displacement field [58] for a dislocation line defect at the center of the atomistic region, and then are relaxed by GF methods according to the forces in GF region. Complete atomistic relaxation is performed in the atomistic region according to the interatomic forces generated from Eq. (1). Forces developed in the GF region, as relaxation is achieved in the atomistic region, are then used to relax those atoms in *all three* regions by the 2D or 3D elastic and lattice GF solutions for line or point forces. The atomistic and GF relaxations are iterated until all force components on each atom are sufficiently small (10^{-4} eV/Å or less), and the final few steps must also be performed by direct atomistic relaxation for the atomistic and GF regions to ensure there is no force build-up in these two regions.

In our GFBC/MGPT simulation code, a spatial domain decomposition scheme is implemented for all three calculational regions, as illustrated schematically in Fig. 2. The small domain cells defined in this scheme are connected via a cell-linked-list method such that each cell has a fixed number of neighboring cells. This reduces the number of unnecessary interatomic separations considered in evaluating the MPGT potentials, which is crucial to their efficient application. In general, there are three major computational issues that need to be addressed: (1) the geometry of the simulation cell, which is purely cylindrical for a straight dislocation and in the form of a series of displaced cylindrical disks for a kink; (2) the fact that there are three regions in the full simulation cell, so that a connectivity algorithm for information passing between different regions is therefore necessary; and (3) the large effective cutoff radius $R_{cut} = 4.25R_{WS}$ for the MGPT potentials, which means there is a large overhead associated with the number of atoms per cell if the conventional domain-cell partition is considered (i.e., if each cell covers a volume R_{cut}^3, which then contains about 16 atoms). To solve these problems, a so-called layered-cake decomposition is used to split the three regions in the full simulation cell, so that each region has it's own domain cell-linked list. To reduce the overhead associated with the number of atoms per cell, the cell sizes are reduced by a factor of eight, therefore the average number of atoms per cell is about

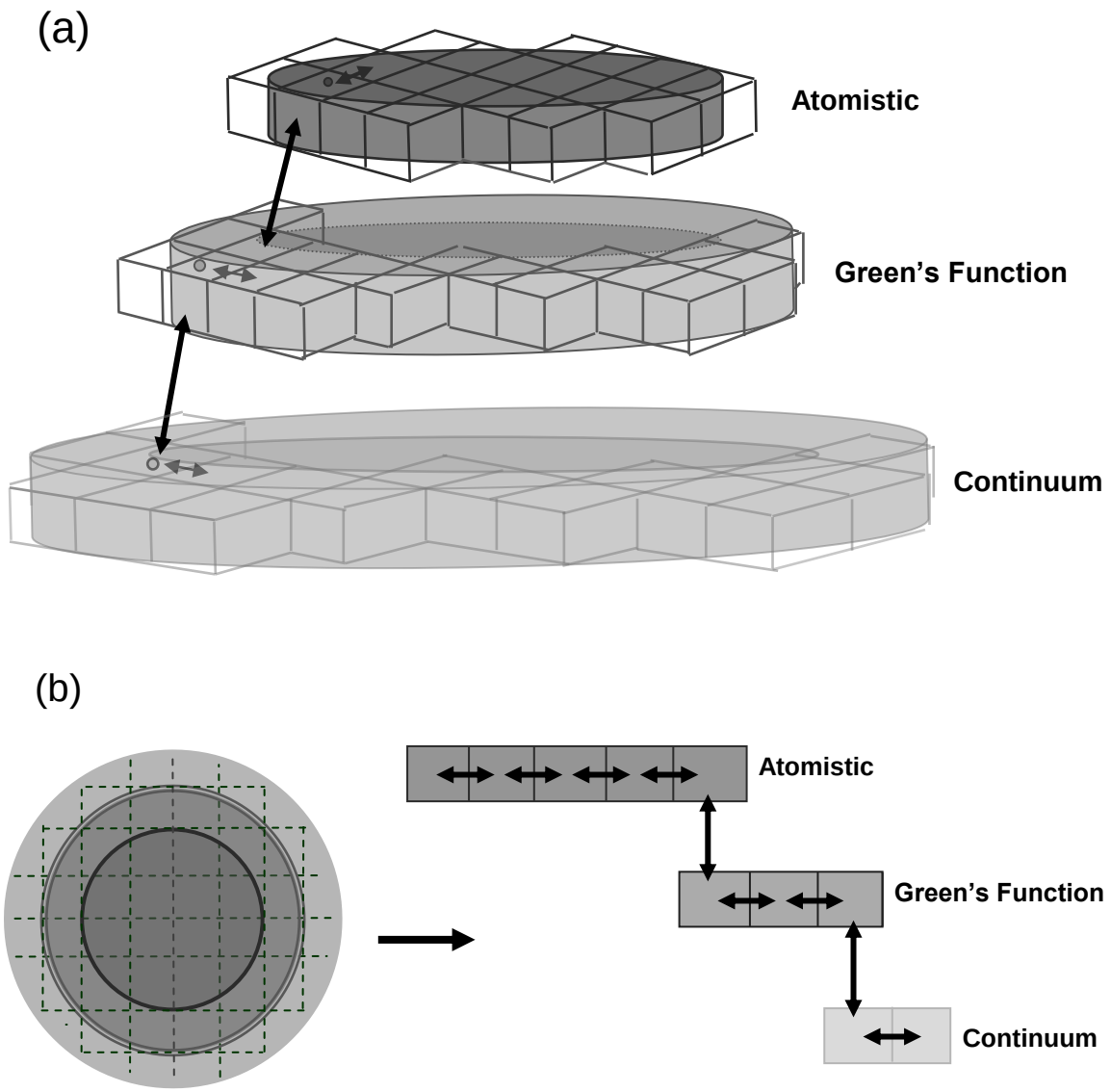

Figure 2. Schematic representation of the domain decomposition scheme used to implement flexible Green's function boundary conditions in our GFBC/MGPT atomistic simulation code for dislocation calculations. (a) The three main computational regions separated into a layered-cake structure for a cylindrical coordinate system such that each region has its own domain decomposition. (b) To ensure the connectivity between regions and compatibility with parallel computing platforms, the domain cells are mapped into three one-dimensional arrays with cell-linked pointers between the cells and overlap regions.

two. In addition, this approach allows a better description of the cylindrical geometry involved in the simulation when a cubic domain decomposition is used. As shown previously [13], the performance of our GFBC/MGPT simulation code is thereby increased by an order of magnitude as compared to conventional domain decomposition methods.

To take advantage of the scalable architectures of modern state-of-the-art computer platforms, a mapping algorithm was also developed for massively parallel computers. A 3D

to 1D mapping list is built at the beginning of the simulation. This mapping list ensures the connectivity between different regions, so that no information is lost during the simulation. The logic behind this algorithm is that our simulation is always performed in a 1D computational domain regardless of the physical geometry involved. This is particular usefully when dealing with complicated geometries such as kinked dislocation structures or dislocation-dislocation interactions.

2.4 Dislocation dynamics simulation

Dislocation dynamics (DD) simulation methods provide a numerical tool to directly connect the physics of individual dislocations to the strength properties of a crystalline material. These methods simulate explicitly the motion, multiplication and interaction of collective dislocation lines in response to an applied load. A number of DD simulation methods have been developed and reported over the past two decades [20-26]. Although they differ in their detailed approach, these methods share in common basic features of dislocation motion and interaction. In this paper, we focus mainly on a general new node-based DD method developed at Lawrence Livermore National Laboratory called ParaDiS (Parallel Dislocation Simulator) that allows efficient large scale DD simulations on parallel computing platforms [27-30]. This approach complements the original lattice-based method for bcc metals of Tang *et al*. [21,22] and here we have performed DD simulations with atomistic input using both methods.

In ParaDiS, the dislocation lines are discretized by an assembly of nodes with straight-line dislocation segments connecting individual nodes [30]. The driving force for dislocation motion is calculated at each node. The force comes from various contributions including the dislocation self-energy change, dislocation-dislocation interaction forces, the external loading, and surface traction forces when applicable [31]. The dislocation-dislocation interactions are treated by isotropic linear elasticity theory and the latest development of non-singular stress expressions [29] has been implemented. A fast multiple method has also been implemented to gain computational efficiency for the force calculations. A detailed description of the ParaDiS method can be found in Ref. 30.

With the nodal forces determined, we calculate the nodal velocities by specifying the response of the nodes to the driving forces through the individual dislocation mobility functions. These mobility functions are very material and environment specific. They require specific parameters obtained from the lower length scale atomistic calculations

performed at the single dislocation level. The mobility functions also depend on the character of the dislocations. In the case of bcc transition metals, the screw and edge mobility functions are defined differently. The screws move primarily by a thermally activated kink mechanism, and the edges move primarily by a phonon drag mechanism. The specific functional forms and parameters of the mobility functions used in our DD simulations are discussed in Sec. 5.1. In the earlier lattice-based DD method, only screw and edge dislocation segments are considered. This method does not provide an accurate description of the dislocation line motion in general, and is only valid for conditions when the screws move much faster than the edges, as occurs in bcc metals at low and moderate temperature. In the current ParaDiS method, on the other hand, we have general line segments connecting the nodes with segment character of all types including screw, edge and mixed segments. The mobility of the mixed segments is derived from that of both screw and edge.

The major material inputs to the DD simulations include the elastic constants and the burgers vector at the chosen pressure and temperature conditions, as well as the pressure-dependent parameters used in the mobility functions. All of these quantities are explicitly calculated at the atomistic level, as described in Secs. 3 and 4 of this paper. The loading conditions for the DD simulations are typically constant strain rate. The major outputs are stress-strain response and the dislocation density changes. In Sec. 5.2, we will discuss the details on the simulation of high pressure yield strengths for Ta and Mo single crystals.

3. Salient High-Pressure Mechanical Properties of bcc Transition Metals

We next discuss some important basic high-pressure mechanical properties of bcc transition metals that both underpin our treatment of dislocations and plasticity and that can be obtained directly from first-principles electronic-structure calculations. These properties includes the bulk and shear elastic moduli, the ideal shear strength, and generalized stacking fault or γ energy surfaces. The pressure-dependent elastic moduli of a material establish the detailed character of the elasticity field in which individual dislocations move and interact, as well as serving as fundamental constraints on our MGPT interatomic potentials. The ideal shear strength provides a fundamental upper bound on material strength in the absence of dislocations and is a basic validation test of the potentials. The relevant low-energy γ surfaces for the {110} and {211} slip planes of interest in bcc plastic flow impose general constraints on dislocation character and are very useful validation tests for the MGPT potentials.

3.1 Bulk and shear elastic moduli

In our treatment of high-pressure mechanical properties, we assume that the bcc solid is subject to a stress tensor of the general form

$$S_{ij} = -P\delta_{ij} + \tau_{ij} \ , \tag{2}$$

where P is the uniform isotropic pressure in the material and τ_{ij} is a small additional applied deviatoric stress. In this regard, we assume that the loading path is such that the material is first uniformly compressed to pressure P through either static (e.g., diamond-anvil cell) or dynamic (e.g., shock) means and then τ_{ij} is applied in some unspecified manner. In transition metals, the pressure $P = P(\Omega, T)$ has a strong dependence on the atomic volume Ω of the metal, but a relatively weak dependence on temperature T. For the purposes of this paper, it is adequate to replace P with the zero-temperature equation of state $P_0(\Omega)$. Calculated MGPT results for $P_0(\Omega)$ and the pressure dependence of the corresponding bulk modulus,

$$B_0(P) = -\Omega \left. \frac{\partial P_0(\Omega)}{\partial \Omega} \right|_{P=P_0(\Omega)} \ , \tag{3}$$

for Ta, Mo and V up to 400 GPa are displayed in Fig. 3. By construction, these results are

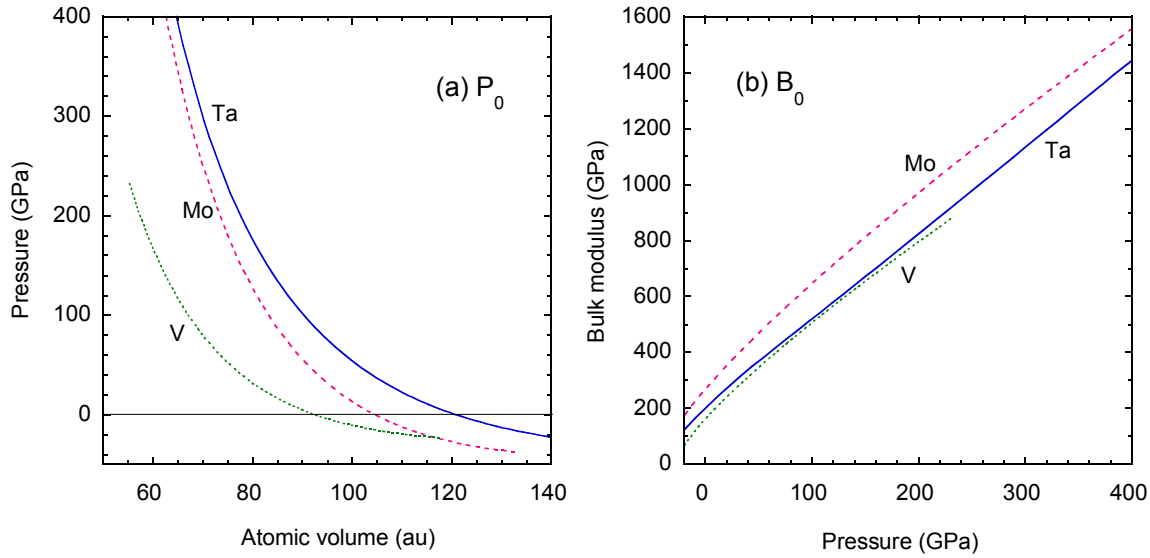

Figure 3. Present calculated zero-temperature equations of state for Ta, Mo and V. (a) Pressure versus atomic volume; (b) bulk modulus versus pressure.

consistent with both room-temperature experimental data [40,54-56] and high-pressure FP-LMTO calculations [37,38,47]. At the observed room-temperature equilibrium volume Ω_0, $P_0(\Omega_0)$ is necessarily slightly negative (~ -1 GPa), as indicated in Table 1 for Ta, Mo and V, since the compensating positive thermal pressure is neglected. In some of our later results we will refer to $P_0(\Omega_0)$ as ambient pressure. Also up to 400 GPa in Ta and Mo and 200 GPa

Table 1. Observed equation of state (EOS) and elasticity properties in Ta, Mo and V at their respective equilibrium volumes [55], with volume in atomic units (a.u.) and stress values in GPa. These data are fully reflected in the present MGPT potentials.

	Quantity	Ta	Mo	V
EOS:				
	Ω_0	121.6	105.1	93.23
	$P_0(\Omega_0)$	-1.1	-1.2	-1.1
	B_0	196	263	157
	B_0'	3.77	4.44	4.26
Elasticity:				
	C_{44}	82.5	109.0	43.4
	C'	52.5	152.0	55.4
	G_{111}	62.5	137.8	51.4
	A	1.57	0.72	0.78

in V, the bulk modulus B_0 is nearly linear in pressure, so that $B_0' = \partial B_0 / \partial P$ is approximately constant over the pressure ranges of interest in this paper. Consistent with the above assumptions and with the usual convention in high-pressure physics, we define individual elastic moduli C_{ij} as stress-strain relations relative to the current compressed state [60]. The corresponding MGPT calculated shear elastic moduli $C' = (C_{11} - C_{12})/2$ and C_{44} are displayed in Fig. 4 for Ta to 1000 GPa, Mo to 400 GPa and V to 250 GPa together with constraining FP-LMTO and experimental data, with equilibrium values listed in Table 1. The experimental data includes ultrasonic measurements of the moduli and their pressure derivatives at ambient conditions [55] and high-resolution inelastic x-ray scattering (HRIXS) measurements at 37 GPa in Mo [56]. The shear moduli generally increase with increasing pressure, except for C' in Mo above 300 GPa and C_{44} in V above 20 GPa. The latter behavior reflects nearby phase transitions: bcc to close-packed phases above 500 GPa in Mo [38,39] and bcc to a rhombohedral phase at 69 GPa in V [40]. In the case of V, C_{44} becomes negative and the bcc structure is mechanically unstable above 120 GPa.

Of special interest here to bcc screw dislocation motion is the effective shear modulus along the <111> slip direction,

$$G_{111} = \frac{2C' + C_{44}}{3} \ , \tag{4}$$

and the corresponding anisotropy ratio,

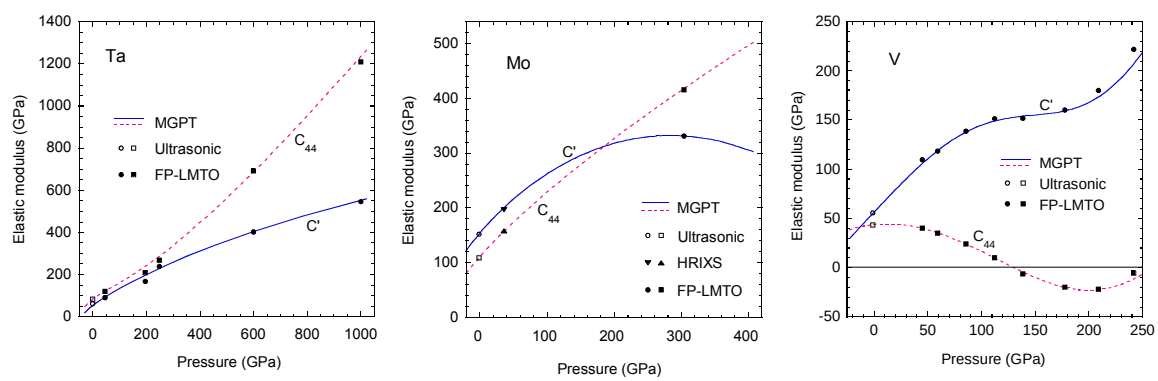

Figure 4. Present MGPT calculated high-pressure shear elastic moduli in Ta, Mo and V together with constraining FP-LMTO and experimental data.

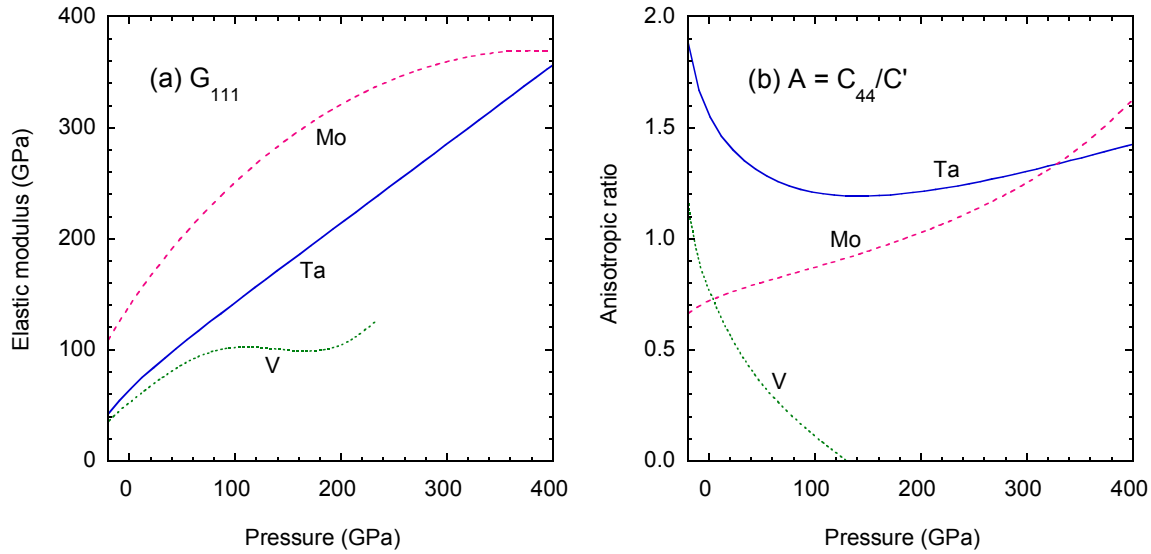

Figure 5. Present calculated high-pressure behavior of the <111> shear modulus G_{111} [panel (a)] and the anisotropic ratio A [panel (b)] for Ta, Mo and V.

$$A = \frac{C_{44}}{C'} \ , \tag{5}$$

where a value of A = 1.0 would denote an elastically isotropic solid. MGPT calculated results on the pressure dependence of these quantities for Ta, Mo and V up to 400 GPa are displayed in Fig. 5. Over this pressure range, G_{111} is nearly linear in pressure for the case of Ta, but has a more complex behavior for Mo and V due to the proximity of the noted phase transitions in these metals. The pressure dependence of A over the same range also shows somewhat complex behavior, with a minimum of about 1.2 in the case of Ta near 140 GPa, a substantial increase with pressure from a value of 0.72 at ambient to about 1.6 at 400 GPa in Mo, and a very rapid decrease with pressure from a value of 0.78 at ambient to zero near 120 GPa in V.

3.2 Ideal shear strength

The next fundamental mechanical property we consider is the ideal shear strength of a bcc metal, as defined by Paxton *et al.* [61] and as previously discussed in the case of Ta [13, 37]. At constant pressure, the ideal strength of the uniformly compressed perfect crystal is identified with the maximum shear stress τ_c required for a continuous homogeneous deformation of the crystal into itself via the observed twinning mode. For bcc metals, this

mode can be specified by a shear direction $\eta = [\bar{1}\bar{1}1]$ and a normal plane $\mathrm{K} = (112)$. In the absence of tensile relaxation normal to K, which has been shown to be small for bcc transition metals [61,62], the atomic positions during the deformation can be directly related to the relative amount of shear x/s along the twinning path, where $s = 1/\sqrt{2}$ is maximum shear displacement along η per unit length along the [112] direction. In particular, the unrelaxed ideal strength calculation may be carried out entirely using a single atom per unit cell and periodic boundary conditions, allowing for easy application of full DFT electronic-structure methods. Previously for Ta, self-consistent FP-LMTO calculations of the unrelaxed ideal shear strength were performed at a few selected volumes in the 0-1000 GPa pressure range [37] and also later repeated at the observed equilibrium volume Ω_0 for comparison with corresponding MGPT calculations [9]. In the present work we have supplemented these results with extensive PP and MGPT calculations as a function of pressure over the range of 0-400 GPa in Ta and Mo and 0-100 GPa in V.

In all cases we calculate a symmetric energy barrier along the twinning path at constant volume,

$$W(x,\Omega) = \frac{E_{tot}[x,\Omega] - E_{tot}[0,\Omega]}{N} \quad , \tag{6}$$

where the barrier height is W_c at $x = s/2$. The corresponding stress along this path is given by

$$\tau(x,\Omega) = \frac{1}{\Omega}\frac{\partial W(x,\Omega)}{\partial x} \quad . \tag{7}$$

The ideal shear strength is then defined as the maximum calculated stress along the twinning path, $\tau_c = \tau(x_c,\Omega)$, where x_c is the critical shear separating regimes of elastic and plastic deformation of the crystal. In the present PP calculations, $W(x,\Omega)$ has been calculated at intervals of $x/s = 0.025$ in the range $0 \le x \le s/2$ and the curve extended to $x = s$ by symmetry. The result has then been fit and differentiated analytically to obtain $\tau(x,\Omega)$ via Eq. (7). In the present MGPT calculations, $W(x,\Omega)$ has been calculated at smaller intervals of 0.01 over the full range $0 \le x \le s$, and then a smooth $\tau(x,\Omega)$ curve has been obtained directly from numerical differentiation. The present PP and MGPT results for Ta at $\Omega = \Omega_0$ are plotted and compared in Fig. 6. Present and previous calculated values of the barrier

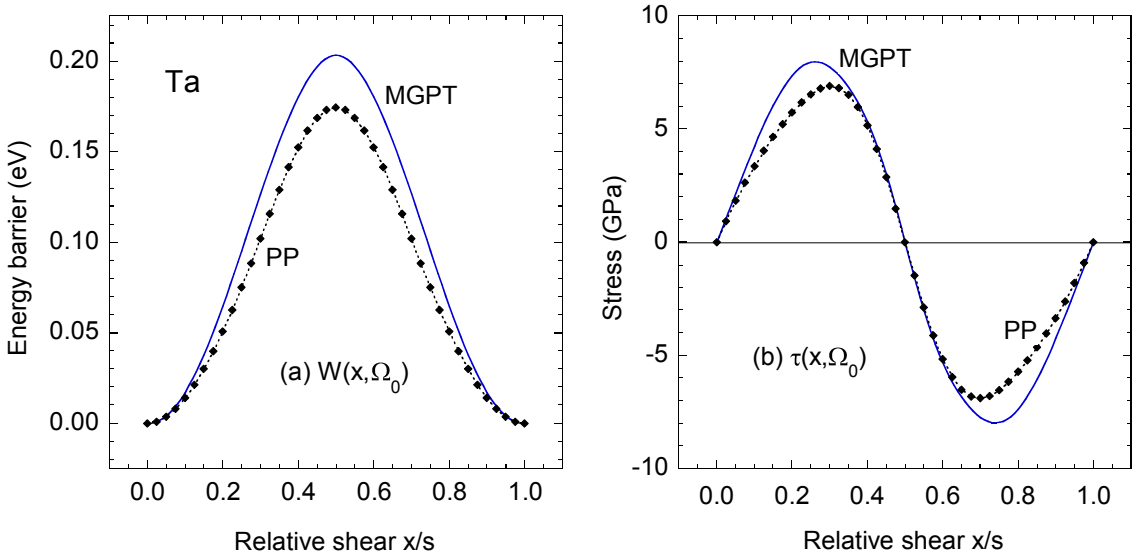

Figure 6. Ideal shear strength of Ta at its observed equilibrium volume Ω_0, as calculated by the PP and MGPT methods. (a) Symmetric energy barrier $W(x,\Omega_0)$; (b) corresponding shear stress $\tau(x,\Omega_0)$.

height W_c, critical stress τ_c, and relative critical shear x_c/s are listed and compared in Table 2 at ambient pressure. The overall agreement among the PP, FP-LMTO and MGPT results is

Table 2. Calculated ideal shear strength properties of Ta, Mo and V at their observed equilibrium volumes, as obtained with the MGPT, FP-LMTO and PP methods.

Metal	Method	W_c (eV)	x_c/s	τ_c (GPa)
Ta:				
	MGPT	0.20	0.26	8.0
	FP-LMTO [(a)]	0.18	0.26	6.5
	PP	0.17	0.30	6.9
Mo:				
	MGPT	0.46	0.27	21.6
	FP-LMTO [(b)]	0.42	0.26	19.2
	PP	0.34	0.25	16.0
V:				
	MGPT	0.15	0.28	7.9
	FP-LMTO [(b)]	0.15	0.26	7.3
	PP	0.09	0.30	5.0

[(a)] Reference 13
[(b)] Reference 61

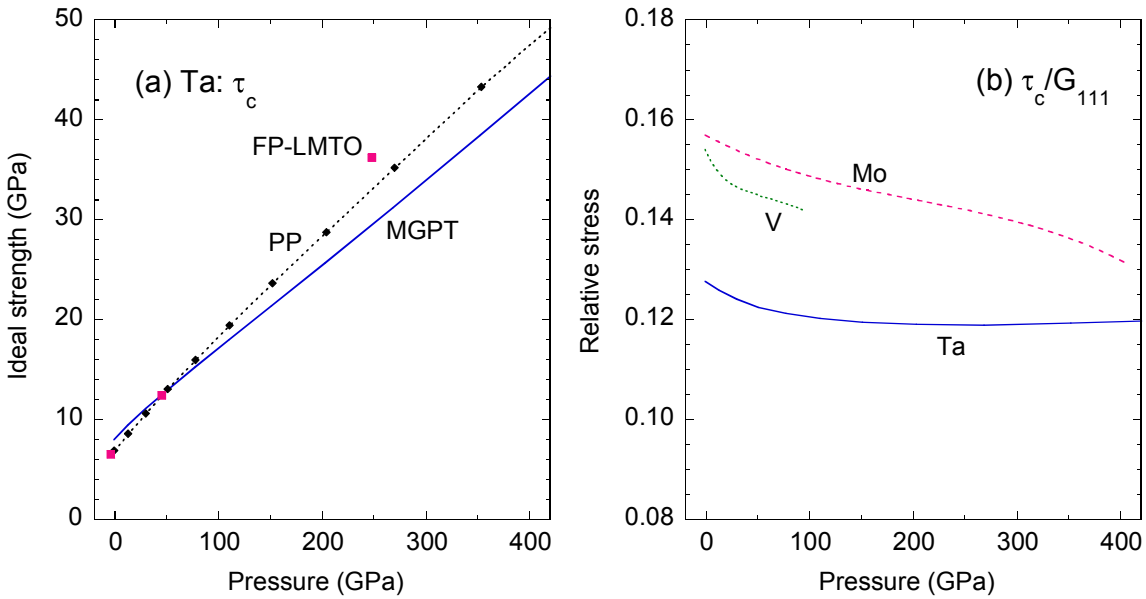

Figure 7. Calculated ideal shear strength in bcc metals at high pressure. (a) Critical stress τ_c in Ta, as obtained with the MGPT, FP-LMTO and PP methods; (b) relative stress τ_c / G_{111} for Ta, Mo and V, as obtained with the MGPT method.

reasonable and adequate for the present purposes, although the MGPT values of W_c and τ_c are systematically larger than the corresponding DFT electronic-structure values and for Mo and V in better agreement with the FP-LMTO results than the PP results.

Under high pressure, the MGPT potentials for Ta, Mo and V also fully capture the qualitative behavior of the ideal strength in these metals, with approximately the same level of quantitative agreement with the DFT electronic-structure calculations as at ambient pressure. In the left panel of Fig. 7, we compare MGPT, FP-LMTO and PP results for the critical stress τ_c in Ta as a function of pressure to 400 GPa. All three results show an approximate linear dependence of τ_c on pressure, as one expects from the linear variation of G_{111} with pressure for Ta displayed in Fig. 5. The MGPT-calculated scaling behavior of τ_c / G_{111} with pressure for Ta and Mo to 400 GPa and V to 100 GPa is plotted in the right panel of Fig. 7. In contrast to the case of Ta, where τ_c / G_{111} remains nearly constant at a value of about 0.12, τ_c / G_{111} for Mo and V shows a noticeable decrease with increasing pressure. In part this reflects the nonlinear variation of G_{111} with pressure for these metals (Fig. 5), although in both Mo and V the variation with pressure is clearly somewhat different for τ_c and G_{111}. At the same time, the variations in τ_c / G_{111} from one material to another as well as under high

pressure for a given material are confined to the small range from 0.12 to 0.16 for all three metals.

3.3 Generalized stacking-fault (γ) energy surfaces

For accurately modeling bcc screw dislocation behavior, an even more important validation test concerns the generalized stacking fault or γ energy surfaces for the {110} and {211} slip planes. As first defined by Vitek [33], the γ surface is an energy profile of two semi-infinite blocks of bulk crystal rigidly displaced relative to each other by a vector ***u*** in a chosen fault plane, with atomic relaxation allowed only perpendicular to the plane. One can calculate high-pressure γ-surface energies at constant atomic volume using an appropriate computational super-cell with periodic boundary conditions. If desired, this can be done using two fault surfaces per super-cell, so that the full translational symmetry of the bulk crystal is preserved. Alternately, one can use one fault surface per triclinic super-cell with two constant lattice translation vectors and a variable vector inclined along the displacement direction ***u***. In this way, the number of atoms needed to define the super-cell is reduced by half, making first-principles DFT electronic-structure calculations of high-symmetry features of the γ surface much more tractable. As previously done in the case of Ta at ambient pressure [13], we follow here the latter approach and use a super-cell consisting of at least 12 atomic planes perpendicular to the fault surface and with one half of the cell shifted by the displacement vector ***u***. In the <111> direction, ***u*** = α ***b***, where $0 \le \alpha \le 1.0$. The same approach can then be applied to MGPT, FP-LMTO or PP calculations at any pressure.

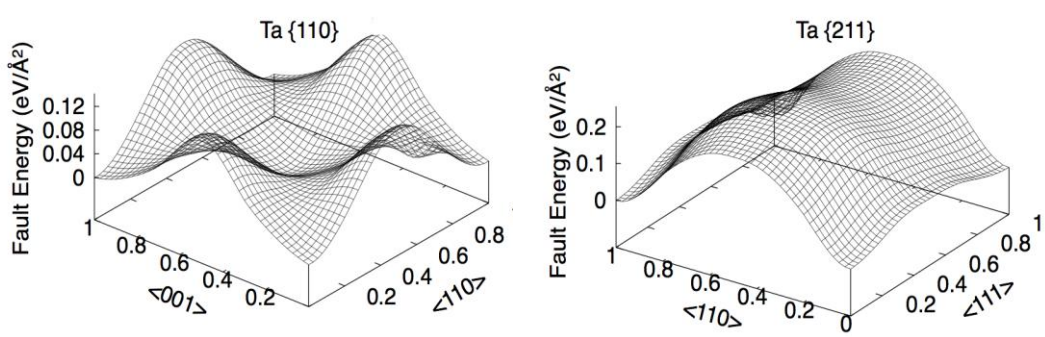

Figure 8. Calculated γ surfaces for Ta at its equilibrium volume $\Omega = \Omega_0$ obtained by the MGPT method. Left panel: the {110} surface; right panel: the {211} surface.

Complete {110} and {211} γ surfaces calculated for bcc Ta at its equilibrium volume with the present MGPT potentials are displayed in Fig. 8. Super-cell size is not a limitation in the MGPT calculations, and larger cells consisting of 32 planes (96 atoms) for the {110} surface and 96 atomic planes (96 atoms) for the {211} surface were used to ensure full convergence. Qualitatively, the calculated γ surfaces display the well known general features expected for bcc metals [33]. In particular, the {110} surface is fully symmetric, while the {211} surface reveals the well known twinning–anti-twinning asymmetry along the <111> direction characteristic of bcc materials. No stable stacking faults in the form of local minima are found on either surface, and all extrema are either maxima or saddle points. These same qualitative features are also maintained in Ta at high pressure to at least 400 GPa, as well as in Mo to 400 GPa and V to 100 GPa.

In order to validate the MGPT potentials quantitatively for high-pressure dislocation studies, we have calculated high-symmetry slices of the {110} and {211} γ surfaces along the <111> direction in Ta, Mo and V using both the MGPT and PP methods. In particular, such calculations along <111> provide a very sensitive test of the quality of the MGPT potentials because the stacking fault energies involved are small and similar in magnitude to those encountered in the formation and motion of $a/2<111>$ screw dislocations. Calculated MGPT and PP results at selected pressures for Ta, Mo and V are shown in Figs. 9, 10 and 11,

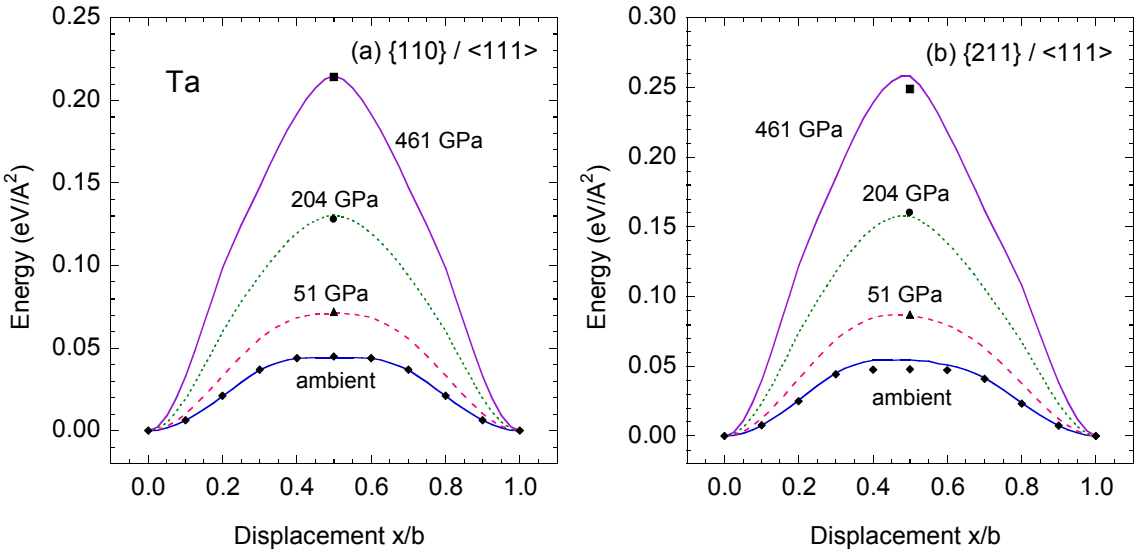

Figure 9. Calculated slices of the {110} and {211} γ surfaces in Ta at four selected pressures obtained using the MGPT (solid lines) and PP (solid points) methods. (a) The {110} surface along the <111> direction; (b) {211} surface along <111>.

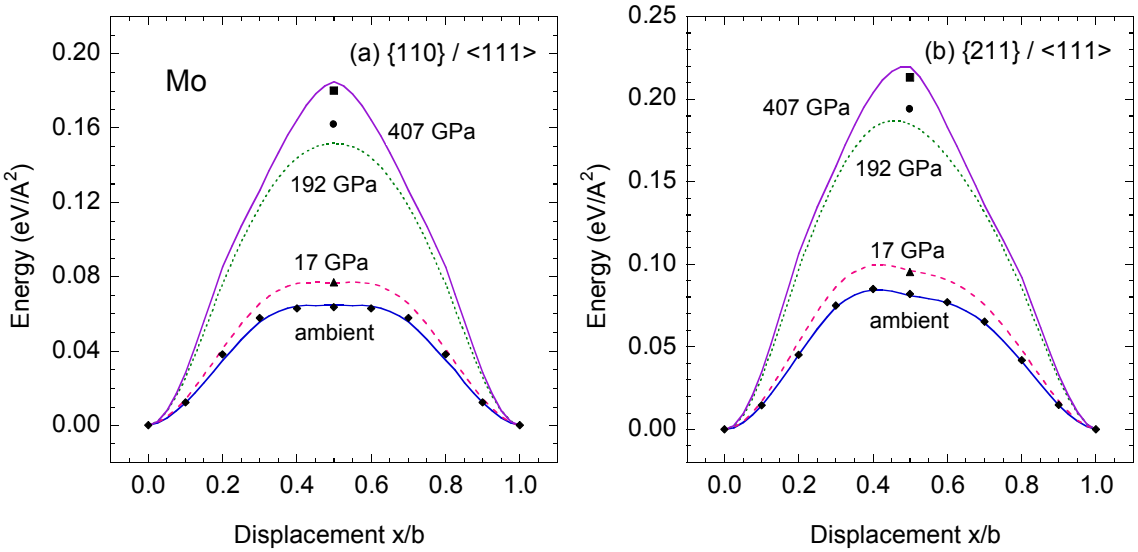

Figure 10. Calculated slices of the {110} and {211} γ surfaces in Mo at four selected pressures obtained using the MGPT (solid lines) and PP (solid points) methods. (a) The {110} surface along the <111> direction; (b) {211} surface along <111>.

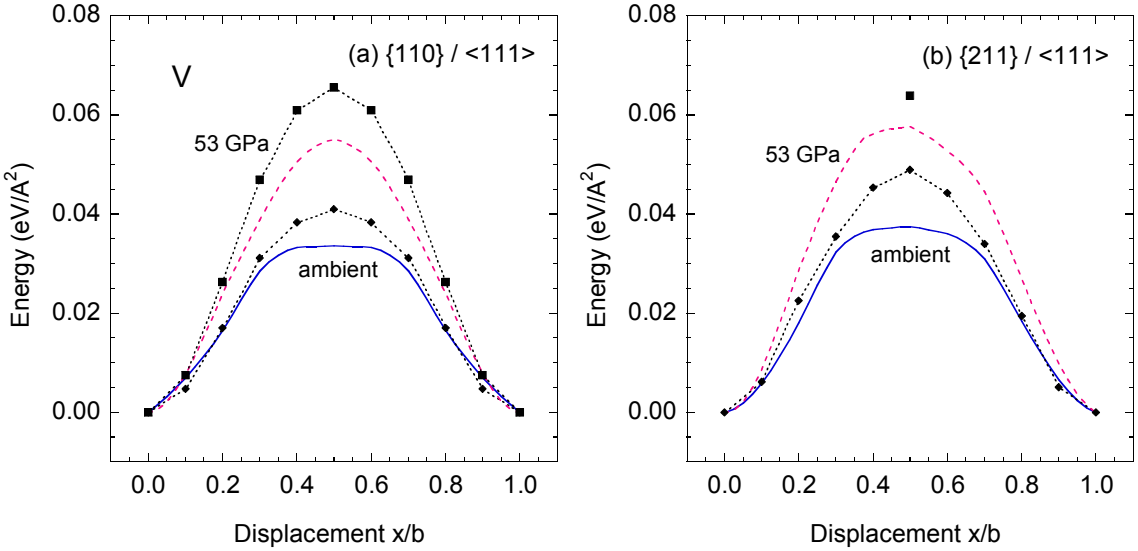

Figure 11. Calculated slices of the {110} and {211} γ surfaces in V at two selected pressures obtained using the MGPT (solid lines) and PP (dashed lines and solid points) methods. (a) The {110} surface along the <111> direction; (b) {211} surface along <111>.

respectively. Here the displacement parameter α can be conveniently written as x/b, where b is the magnitude of the Burgers vector. In the cases of Ta and Mo, the maxima in these curves at $x = b/2$, which is commonly defined as the unstable stacking fault energy γ_{us}, increase monotonically with pressure. This is shown more directly in Fig. 12(a) where complete MGPT results for γ_{us}^{110} and γ_{us}^{211} are plotted as a function of pressure up to 400 GPa. At each of the selected pressures in Figs. 9 and 10, the MGPT curves conform to the PP points very closely and the quantitative agreement is everywhere within 7%. In this regard, on the {211} γ surface of Mo the expected twinning–anti-twining asymmetry is clearly evident in both the MGPT and PP results, and is very accurately predicted by the MGPT potentials. We conclude, therefore, that the present MGPT potentials should be reliable for the calculation of the $a/2<111>$ screw dislocation properties for Ta and Mo up to at least 400 GPa.

The case of V shows somewhat more complicated behavior. In this metal the calculated PP and MGPT stacking fault energies increase monotonically with pressure only up to about 80 GPa such that above that point the γ surface actually lies lower in energy than that at 53 GPa. This is shown more clearly in Fig. 12(a), where the complete set of MGPT unstable stacking fault energies γ_{us}^{110} and γ_{us}^{211} for V up to 230 GPa are plotted. In addition, up to at least 53

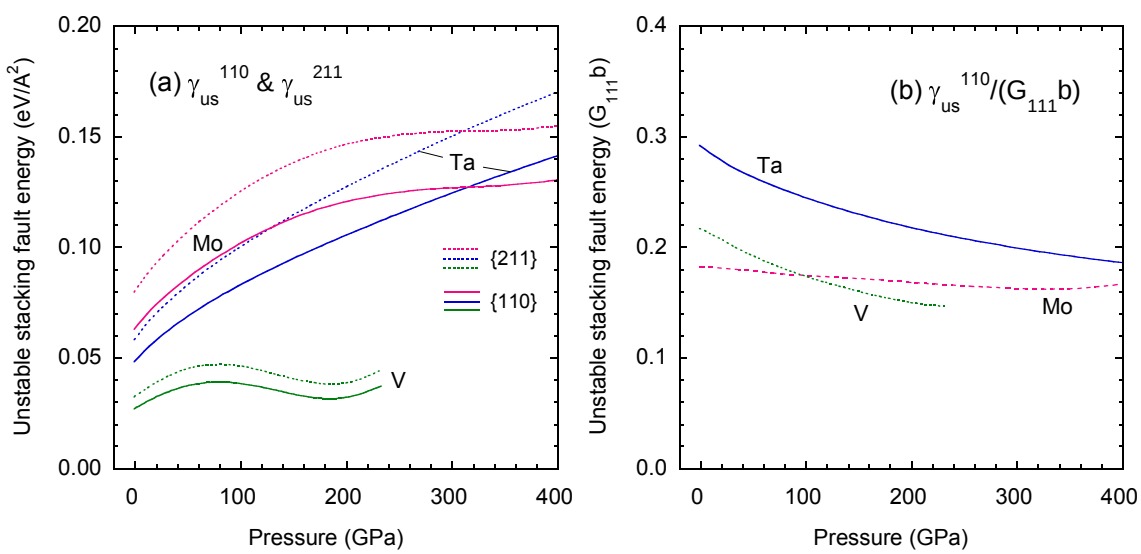

Figure 12. Unstable stacking fault energies for Ta, Mo and V, as calculated with the MGPT method. (a) Energies γ_{us}^{110} and γ_{us}^{211} for the {110} and (211} γ surfaces, respectively; (b) scaled energy $\gamma_{us}^{110}/(G_{111}b)$ for the {110} surface.

GPa, the calculated PP stacking fault energies are systematically higher than those obtained with the MGPT potentials by 10-25%, as shown in Fig. 11. This makes the MGPT calculation of $a/2<111>$ dislocation properties in V somewhat less certain quantitatively than in either Ta or Mo.

Figure 12(a) further shows that the {110} unstable stacking fault energy γ_{us}^{110} is systematically smaller than the {211} fault energy γ_{us}^{211} for all pressures up to 400 GPa in Ta and Mo and up to 230 GPa in V. This has important implications for the motion of $a/2<111>$ screw dislocations on {110} and {211} slip planes. At all pressures considered here, the screw dislocations in Ta, Mo and V prefer to move on {110} planes for Ta, Mo and V, although, as previously discussed [13], this can happen in more than one way, such that at larger length scales slip may effectively appear to occur on either {110} or {211} planes. Also the scaled fault energy $\gamma_{us}^{110}/(G_{111}b)$ displays scaling properties similar to those found for the scaled ideal strength τ_c/G_{111}, except that the roles of Ta and Mo are reversed, as shown in Fig. 12(b). In particular, the scaled unstable stacking fault energy is nearly constant as a function of pressure in the case of Mo, but clearly decreases with pressure for Ta and V.

4. *a*/2 <111> Screw Dislocation Properties at High Pressure

As first pointed out by Hirsch [63], the mobility of an $a/2<111>$ screw dislocation in a bcc lattice is severely restricted by the atomic structure of its core. Around a given <111> direction, the bcc structure has three-fold symmetry. Each such <111> zone contains three {110} and three {112} planes that are potential slip planes in the bcc structure, as well as admitting the possibility of a three-dimensional spreading of the core structure along <112> directions on the {110} planes when the screw dislocation is formed. Detailed descriptions of extended core structures in bcc metals have been obtained from many previous atomistic studies [9-19,32-36,64] and have indicated a core extension of a few Burgers vectors in length and a high Peierls stress associated with its movement under an applied load. In this section, we discuss our atomistic simulations of basic $a/2<111>$ screw dislocation core properties at both ambient and high pressure in bcc Ta, Mo and V, using the MGPT potentials and Green's-function methodology discussed above. Our focus will be on the zero-temperature calculation of core properties that are fundamental to an understanding of dislocation structure and mobility. The properties considered include the atomic structure and energy of the equilibrium dislocation core in the absence of any additional shear stress, the nature and energetics of isolated kinks and mobile kink pairs that can be formed from this core in the low shear stress limit, and the magnitude and orientation dependence of the Peierls stress required to move the rigid dislocation in the high shear stress limit. To link directly to corresponding DD simulations of plasticity, we also consider the full activation enthalpy associated with activated screw dislocation motion as a function of applied shear stress, as well as dislocation motion above the Peierls stress in the phonon drag regime.

4.1 Equilibrium core structure and energy

The $a/2<111>$ screw dislocation has one or more stable core configurations located at the center of gravity of three <111> atomic rows forming a triangular prism. Around these three rows the near-neighbor atoms are located on a helix that winds up in a clockwise or counter-clockwise manner, depending on the location of the elastic center and the sign of the Burgers vector, so that two different types of core configurations can be obtained [9]. One configuration is isotropic and of high energy and may or may not be stable. This is usually referred to as the “hard” core. The other configuration is of low energy and is normally the stable ground-state structure. This is the so-called “easy” core. In general, the “easy” core can exhibit three-fold <112>/{110} directional spreading in two geometrically distinct, but energetically equivalent ways, resulting in a doubly degenerate ground-state core structure with two possible orientations. Under certain circumstances, however, this directional

spreading may vanish and an isotropic non-degenerate core with a higher, but still three-fold, symmetry results. In the present work, we have studied the pressure dependence of the "easy" core ground-state in bcc Ta, Mo and V up to very high pressure.

As done previously [13,14,16,19], we have simulated the stable ground-state screw dislocation core structure using a two-dimensional GFBC/MGPT technique in cylindrical geometry, with periodic boundary conditions and a period of $b = \sqrt{3}a/2$ along the *z* axis (<111> direction) at constant atomic volume $\Omega = a^3/2$ in the bcc structure. In this procedure, an infinite $a/2<111>$ screw dislocation is first introduced by displacing all atoms in the simulation according to anisotropic elasticity solutions using Stroh's sextic formalism [58]. The atomic positions of the core atoms are then allowed to relax within the GFBC simulation cell. Radially outward from the cylinder axis, the inner atomistic region of the simulation cell is surrounded by GF and continuum regions (see Fig. 2) each with a shell thickness of $R_{cut} = 4.25R_{WS}$, the effective cutoff radius for the MGPT potentials. A radius for the atomistic region of about 20*b* is needed to accurately characterize the fully relaxed core structure.

The qualitative aspects of the calculated core structures are most easily displayed and discussed using the standard differential displacement method of Vitek [33]. In this method, the <111> screw components of the relative displacement of neighboring atoms due to the dislocation (i.e., the total relative displacement in the *z* direction less than that in the perfect lattice) is represented by an arrow between the two atoms. The calculated screw-component differential displacement maps for Ta at two widely different pressures are shown in Fig. 13. The left panel of that figure displays the nearly isotropic core structure of Ta that we calculate at ambient pressure, while the right panel shows the strong directional spreading obtained in the same metal at a pressure of 1000 GPa. In both cases, the length of the arrows is normalized by $b/3$, the magnitude of the separation of neighboring atoms along the <111> direction. A corresponding differential displacement map can also be constructed for the edge components of the dislocation as well, but the magnitude of the edge displacements is found to be 10-100 times smaller than that of the screw components [13], and we do not consider these further in this paper.

Qualitatively, the core structures displayed in Fig. 13 are representative of the isotropic and the spread core structures we have obtained for Ta, Mo and V. The degree of three-fold directional spreading of the core can be directly quantified by its so-called polarization ***p,*** which measures the simultaneous translation of the three central atoms nearest to the core

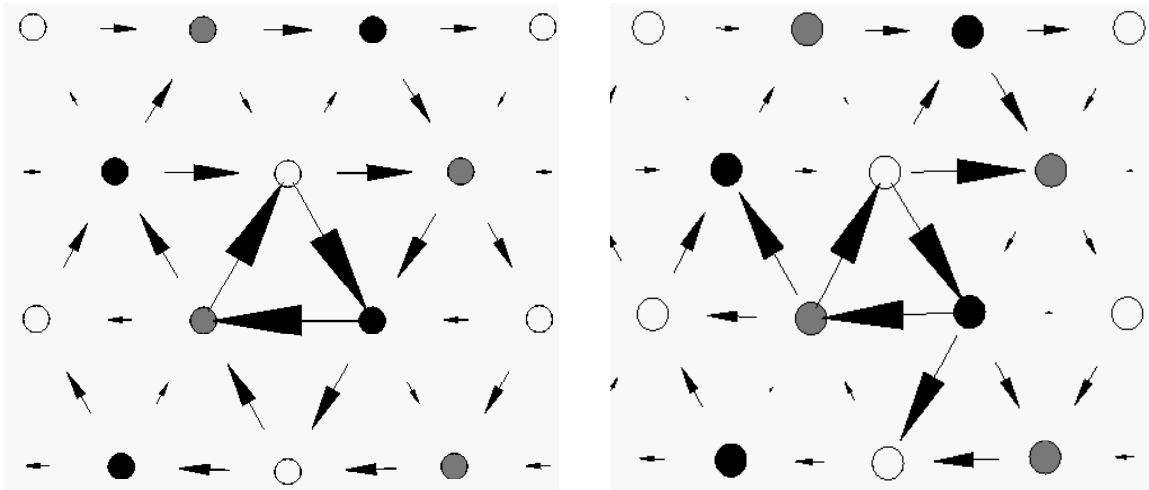

Figure 13. Differential displacement maps of the relaxed core structures of Ta at low and high pressure as calculated with GFBC/MGPT atomistic simulations. Left panel: isotropic core structure at ambient pressure; right panel: spread core structure at 1000 GPa.

center [64,65]. This translation is parallel to the dislocation line but in the opposite sense for the two different core orientations, usually denoted as positive *p* and negative *n*. By symmetry, the magnitude of *p* can only vary zero to *b*/6. At *p* = 0, the two core configurations coincide and a fully symmetric or isotropic core structure with a higher three-fold symmetry is obtained. At *p* = *b*/6, on the other hand, a fully polarized core is obtained with a maximum three-fold spreading along <211> directions. Our calculated core polarization as function of atomic volume and pressure is plotted in Fig. 14 for Ta and Mo to 400 GPa and in Fig. 15 for V to 75 GPa. In the cases of Ta and Mo near equilibrium ($\Omega = \Omega_0$) and at expanded volumes corresponding to negative pressures, the calculated core polarization is less than 0.02*b*/6, the approximate level of accuracy of our results, and thus consistent with a non-degenerate isotropic core structure. Under compression, however, the polarization rises rapidly in both cases and attains a value of 0.5*b*/6 near pressures of 400 GPa. In contrast to Ta and Mo, the dislocation core of V is already significantly polarized near equilibrium and *p* rises only to a maximum of about 0.275*b*/6 near 32 GPa and then descends rapidly toward zero close to the bcc $\rightarrow$ rhombohedral phase transition observed at 69 GPa [40]. As in Ta and Mo, at sufficiently expanded volumes and negative pressure in V, the polarization *p* does tend toward zero. In all three metals, the transition between an isotropic core with *p* = 0 and a spread core with finite *p* appears to be continuous and not a first-order phase transition. Calculated values of *p* at $\Omega = \Omega_0$ for Ta, Mo and V are listed in Table 3.

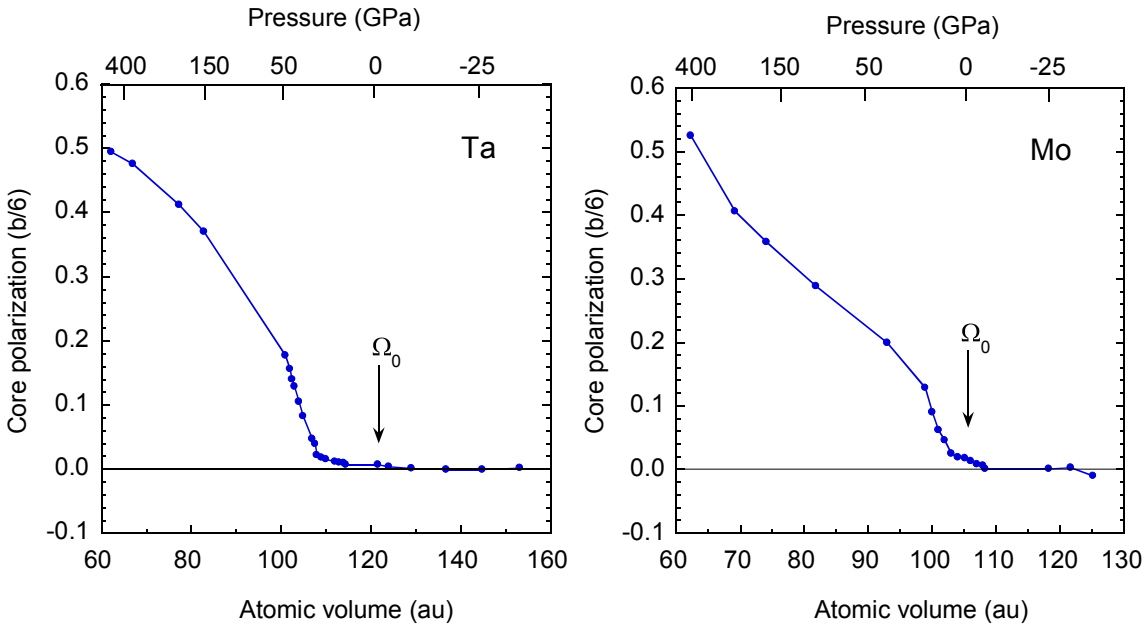

Figure 14. Calculated volume and pressure dependence of the core polarization for Ta and Mo, as obtained from the present GFBC/MGPT atomistic simulations.

The above results show clearly that the screw dislocation core structure in bcc metals is a materials specific property that depends both on chemical element and environmental factors

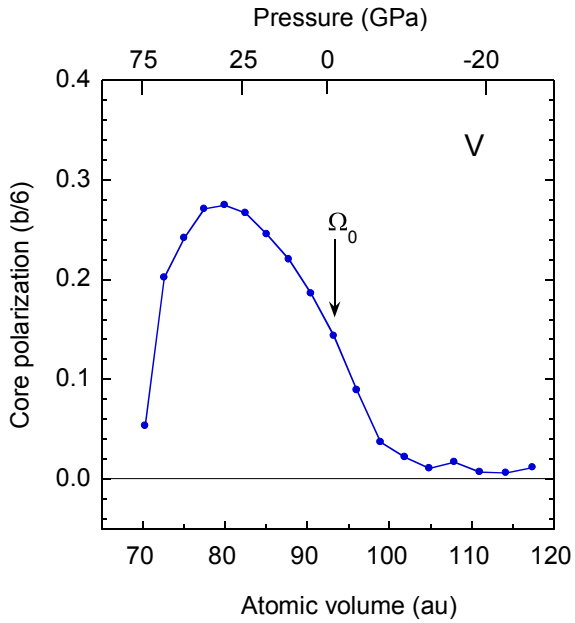

Figure 15. Calculated volume and pressure dependence of the core polarization for V, as obtained from the present GFBC/MGPT atomistic simulations.

Table 3. Basic $a/2<111>$ screw dislocation properties in bcc Ta, Mo and V at their respective equilibrium atomic volumes [55]. Included quantities are the atomic volume Ω_0; bcc lattice constant *a*; magnitude of the Burgers vector *b*; core polarization *p*; core radius R_c; core energy E^f_{core}; elastic energy $A_{elastic}$; kink-pair formation energy E^f_{kp}; and Peierls stress τ_P.

	Quantity	Ta	Mo	V
Structure:				
	Ω_0 (Å^3)	18.02	15.57	13.82
	a (Å)	3.303	3.146	3.023
	b (Å)	2.861	2.725	2.618
	p (*b*/6)	0.007	0.018	0.144
Energy:				
	R_c/b	1.75	1.75	2.0
	E^f_{core} (eV/Å)	0.22	0.30	0.11
	$A_{elastic}$ (eV/Å)	0.25	0.50	0.17
Mobility:				
	E^f_{kp} (eV)	0.96	1.15	0.68
	τ_P (GPa)	0.577	0.860	0.360
	τ_P/G_{111}	0.00923	0.00625	0.00701

such as pressure. Near ambient pressure, our predictions of a nearly isotropic core structure in Ta and Mo are consistent with recent first-principles DFT electronic structure calculations of core structure using small computational cells and a variety of boundary conditions [10,11,17,66], as well as with quantum-based bond-order potential (BOP) calculations on Mo using fixed boundary conditions [18]. In contrast to our results for Mo and V, an earlier systematic study of the Group-VB and -VIB metals using empirical radial-force potentials [29] found isotropic cores for the VB metals, including V and Ta, and three-fold spread cores for the VIB metals, including Mo. Our present result for Mo at ambient pressure is also in contrast to previous results [9,12] which found a strong three-fold spreading of the core structure using the earlier generation 1994 MGPT potentials for that metal [50].

In addition to its atomic structure, it is also of interest to calculate the effective size and energy associated with the equilibrium core, as done previously for Ta at ambient pressure [13]. In continuum elasticity theory, the formation energy E^f_{screw} of a screw dislocation (per unit length) in a cubic crystal is a linear function of $\ln(R/R_c)$, where *R* is the outer radius of a cylinder which contains the dislocation core at its center and R_c is the core radius. The formation energy E^f_{screw} includes the core energy stored inside R_c, E^f_{core}, plus the elastic energy stored in the region between R_c and *R*, such that

$$E^f_{screw} = E^f_{core} + A_{elastic} \ln\left(\frac{R}{R_c}\right) , \tag{8}$$

where the elastic energy coefficient $A_{elastic}$ can be directly calculated from the elastic moduli of the material [9]. The main unknown in Eq. (8) is the minimum core radius R_c that will satisfy that equation. This can be found by iteration, starting with a trial value of R_c and calculating E^f_{core} and E^f_{screw} via atomistic simulation as a function of *R*. An essentially equivalent procedure that is sometimes useful in the context of GFBC/MGPT simulations is to define R_c to be the minimum radius at which the 2D elastic and lattice Green's functions become equal [13]. Either procedure results in some uncertainty in determining optimum values of R_c, but here we have used the former approach and thereby calculated E^f_{core} for selected pressures in Ta, Mo and V. In all three metals, we determine R_c / b to be in the range 1.75-3.0, with R_c increasing with increasing pressure up to 400 GPa. Our calculated results for E^f_{core} and $A_{elastic}$ are plotted in Fig. 16 with the ambient pressure results for R_c / b, E^f_{core} and $A_{elastic}$ given in Table 3. As seen in Fig. 16, the uncertainty in R_c results in some fluctuations in the calculated values of E^f_{core}.

4.2 Low shear stress limit: kink-pair formation energy

At finite temperature, the motion of the screw dislocations in the bcc lattice normally occurs by the thermally assisted formation and migration of kink pairs. For low shear stress conditions, the individual kinks in a kink pair are well separated and weakly interacting, so kink-pair formation can be modeled by just looking at isolated left and right kink formation. In this limit, the nature and atomic structure of the possible kinks is closely related to the unstressed dislocation core, which we assume here is of doubly degenerate form. As we have discussed above, the doubly-degenerate core structure of the rigid $a/2<111>$ screw dislocation can have two energetically equivalent configurations with opposite polarizations denoted as positive *p* and negative *n*. As a result, there are different possible kinks and kink-pair configurations involving *p* and *n* segments that can be formed. In addition, *p* and *n* segments can co-exist on the same dislocation line in the form of a so-called anti-phase defect (APD). This further increases the multiplicity of possible kinks and kink pairs, as we have previously elaborated in the case of Ta [13].

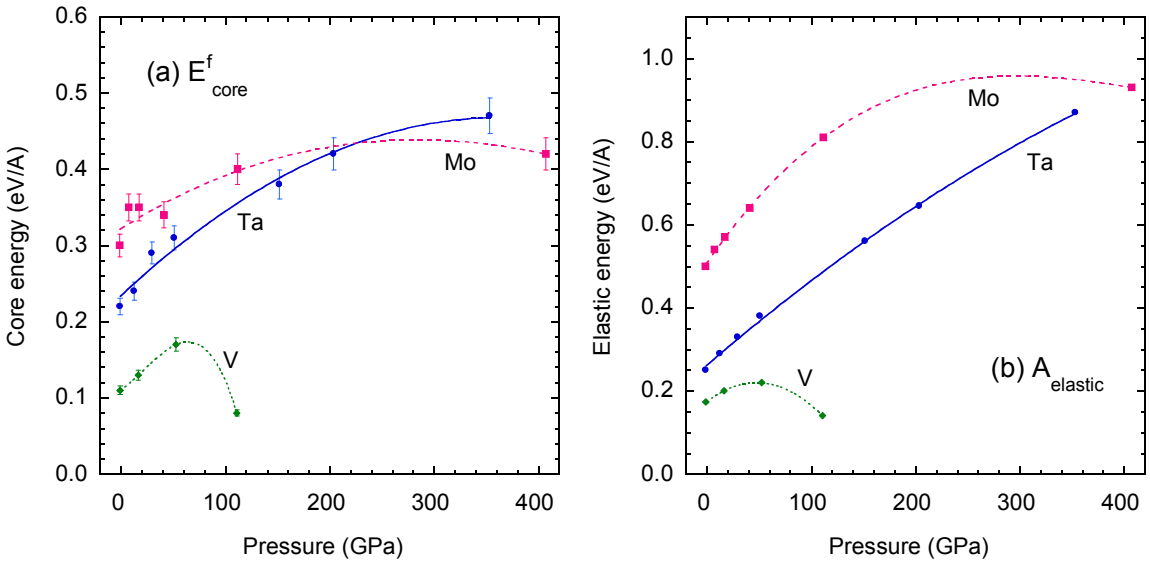

Figure 16. Core and elastic contributions to the screw dislocation formation energy [Eq. (8)] in Ta, Mo and V as function of pressure. (a) Core formation energy E^f_{core} as obtained from GFBC/MGPT atomistic simulations; (b) elastic coefficient $A_{elastic}$ determined from MGPT elastic moduli.

Here we assume that an isolated left (*l*) or right (*r*) kink of a kink pair consists of two semi-infinite segments of *p* or *n* orientation separated by a kink height *h*. The symmetry of the bcc lattice allows six distinct and non-degenerate kinks [34]. These are of character *nln* (degenerate with *plp*), *nrn* (degenerate with *prp*), *nlp*, *nrp*, *pln* and *prn*. As previously demonstrated in the case of Ta [13], the lowest energy kink pair in the absence of a pre-existing APD has the character *pln-nrp*. In Ta at ambient pressure and zero applied shear stress, this kink pair has a calculated formation energy E^f_{kp} of 0.96 eV, which is close agreement with the empirically derived zero-stress activation enthalpy of 1.02 eV used in microscale DD simulations to account for the observed yield stress [21]. For this reason, we have adopted the *pln-nrp* kink pair as the appropriate model for kink pair formation in bcc transition metals and used it here for Ta, Mo and V at both ambient and high pressure.

To model an isolated *pln or nrp* kink accurately, we work at constant volume and set up the GFBC simulation cell in the form of a long compliant cylinder made up of unit disks of width *b* and radius 20*b* (for the atomistic region) and a total length 60-80*b* centered on the dislocation line. A transition region of 10-15*b* is allowed across the kink height *h*, where the kink is fully relaxed in the GFBC/MGPT simulation. To form a closed 3D cage, the two ends of the cylinder are capped with GF and continuum regions. The z-axis of the compliant cylinder is taken parallel to a [111] dislocation line direction, while the y-axis is taken

parallel to $[1\bar{1}0]$ and the x-axis to $[\bar{1}\bar{1}2]$. The smallest repeat translation vector for the rigid screw dislocation core in the bcc lattice is $(a/3)[\bar{1}\bar{1}2]$ on a $\{110\}$ plane, and this defines the elementary kink height h with magnitude $\sqrt{6}a/3$. We have considered only kinks formed within this geometry. Kinks formed on other planes such as $\{211\}$ have significantly larger kink heights and therefore are either unstable or have much larger kink formation energies [9,67].

We further assume that the process of kink-pair formation is limited by the isolated kink formation energies E^f_{pln} and E^f_{nrp}, as opposed to the competing process of kink migration, which is controlled by the secondary Peierls stresses needed to move the left- and right-hand kinks. As shown previously in the case of Ta at ambient pressure [13], the secondary Peierls stresses are one to two orders of magnitude smaller than the corresponding Peierls stress for the rigid screw dislocation itself, so both kinks are expected to be mobile with the left kink moving faster than the right kink. Consequently, we expect the dislocation velocity at low shear stress τ to be controlled by the kink-pair formation energy E^f_{kp} rather than any small kink migration barriers. In the $\tau = 0$ limit, the former is calculated as a sum of left- and right-kink formations energies:

$$E^f_{kp} = E^f_{pln} + E^f_{nrp} \quad . \tag{9}$$

The individual left and right kink formation energies are most efficiently calculated by summing the unit disk contributions in our GFBC compliant cylinder across the transition region in the kink. That is, in each unit disk we subtract from the atomistic total energy with the kink present the corresponding total energy for the perfect straight dislocation. This procedure provides a cancellation of total-energy errors and leads to kink-formation energy values that are typically accurate to 0.05-0.10 eV or 5-10%. We have so calculated E^f_{kp} at selected pressures in Ta, Mo and V. These results are plotted in Fig. 17(a) with ambient-pressure values listed in Table 3. As expected, E^f_{kp} is monotonically increasing with pressure, but in a significantly nonlinear way in each case. The scaled kink-formation energy $E^f_{kp}/(G_{111}b^3)$ displays a somewhat soother and slowly varying pressure dependence in the cases of Ta and Mo, as shown in Fig. 17(b). In any case, the calculated values of E^f_{kp} constrain the low shear stress limit of the full stress dependent activation enthalpy for dislocation motion, which is considered below in Sec. 4.4.

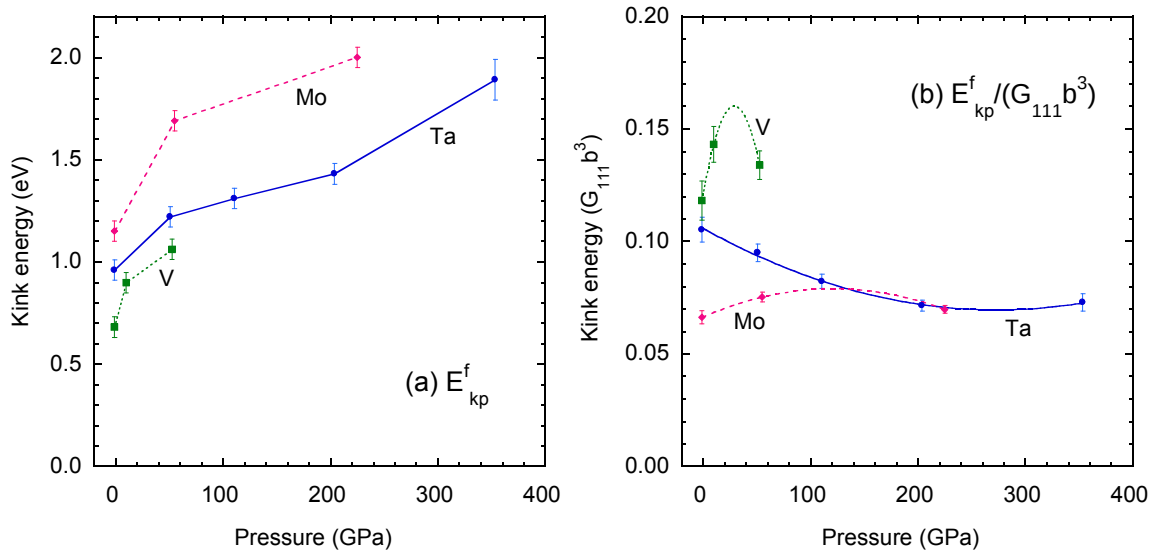

Figure 17. Pressure dependence of the *pln-nrp* kink pair formation energy for Ta, Mo and V, as calculated from GFBC/MGPT atomistic simulations. (a) Full energy E_{kp}^{f}; (b) scaled energy $E_{kp}^{f}/(G_{111}b^3)$.

4.3 High shear stress limit: Peierls stress

Next we turn to the high stress limit and the calculation of the Peierls stress τ_P for the rigid $a/2<111>$ screw dislocation. Bcc metals are known to slip predominantly on {110} and/or {112} planes at low temperatures, but this slip does not follow the familiar Schmid law [68] and, in fact, a rather complex orientation dependence of the slip geometry and the yield stress is experimentally observed [69]. Consequently, one expects that there is a strong dependence of the critical resolved shear stress (CRSS) needed to move the rigid screw dislocation on the orientation of the applied stress. In the context of GFBC/MGPT simulations, this orientation dependence was previously investigated in bcc Ta at ambient pressure [13] by applying both pure glide shear stresses and selected shears with a uniaxial stress component. For applied stresses on either a {110} plane or in the twinning direction of a {112} plane, it was found that the addition of a uniaxial stress component in either compression or tension always raises the CRSS. For this reason, we have confined our attention here to only applied shear stresses and have examined the CRSS in both Ta and Mo at ambient pressure. For our present purposes we identify the Peierls stress τ_P with the minimum CRSS as a function of shear stress orientation and then calculate the pressure dependence of τ_P for that orientation.

In order to determine the Peierls stress in a self-consistent and accurate manner, our GFBC/MGPT simulations of the CRSS have been performed at conditions of constant stress, rather than at constant volume, and start from the relaxed equilibrium core structure as determined above. The simulations do utilize periodic boundary conditions along the screw axis, however, so they are strictly 2D zero temperature calculations. For a given applied stress orientation, the CRSS is assumed to be reached when the dislocation moves at least one lattice spacing on the maximum resolved shear stress plane. In a bcc crystal along a given <111> direction, there are three {110} planes and three {112} planes, mutually intersecting every 30°. Because of the twinning–anti-twinning asymmetry in the bcc lattice, unique values of the CRSS can exist on different planes ranging in orientation from χ = -30° (twinning orientation on {211}) to χ = 30° (anti-twinning orientation on {211}), with χ being the angle measured from a given {110} slip plane. The CRSS over this orientation range has been calculated in Ta and Mo at ambient pressure and the results are presented in Fig. 18. In the case of Ta, these results are the same as those reported previously [13] except at χ = 0, where the CRSS is calculated slightly lower in value. Both Ta and Mo display a significant twinning–anti-twinning asymmetry with the minimum CRSS occurring at χ = 0°. These latter results are our defined values of τ_P at ambient pressure and are also listed in Table 3.

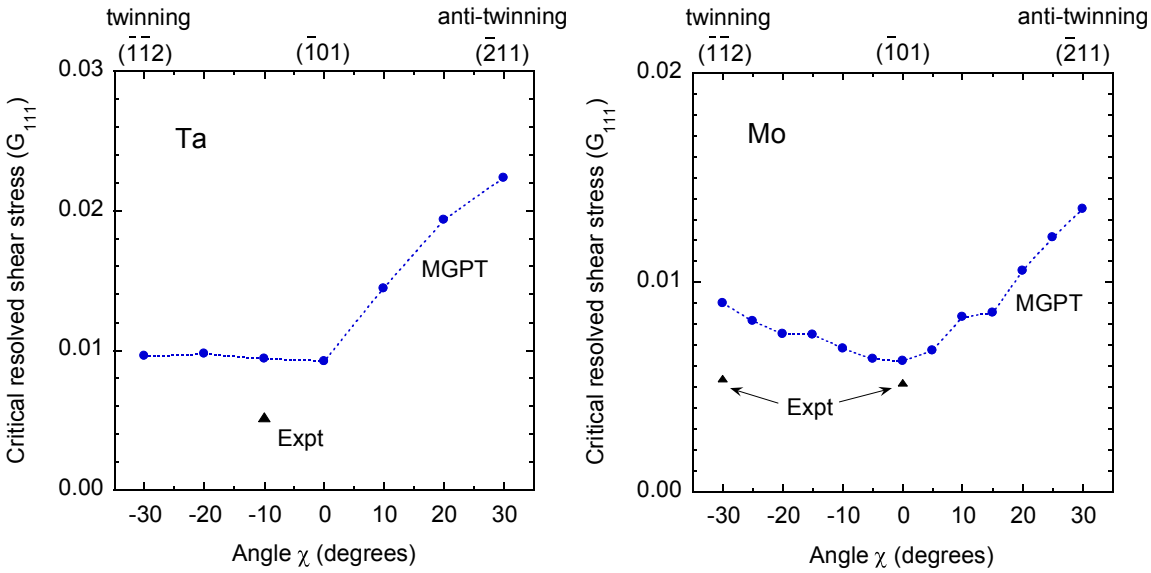

Figure 18. Orientation dependence of the critical resolved shear stress (CRSS) in Ta and Mo at ambient pressure, as calculated with the present MGPT potentials and compared with experimental estimates based on the observed yield stress [70-72].

Also plotted for comparison in Fig. 18 are experimental estimates of the CRSS or Peierls stress based on the observed yield stress at the indicated stress orientations [70-72]. In the case of Ta at χ = -10° and Mo at χ = -30°, our calculated CRSS values are nearly a factor of two greater than the experimental estimates, while in Mo at χ = 0° our result is only about 20% higher. However, experiment here does not represent a direct measurement of the Peierls stress, and consequently, the relationship between theory and experiment remains an open and somewhat controversial question [13,16]. Also is this regard, other recent quantum-based calculations of the same CRSS in Ta and Mo produce generally higher values than ours [15,16,18]. These include small-cell DFT calculations using Green's function boundary conditions [15] as well as larger-cell BOP calculations with fixed boundary conditions [18]. Whether or not these differences represent a sensitivity of the calculations to cell size and/or boundary conditions also remains an open question.

We have obtained the pressure dependence of the Peierls stress by performing GFBC/MGPT simulations of the χ = 0° CRSS for selected pressures to 1000 GPa in Ta, to 400 GPa in Mo and to 53 GPa in V. The resulting scaled Peierls stress τ_P / G_{111} is plotted for Ta and Mo in

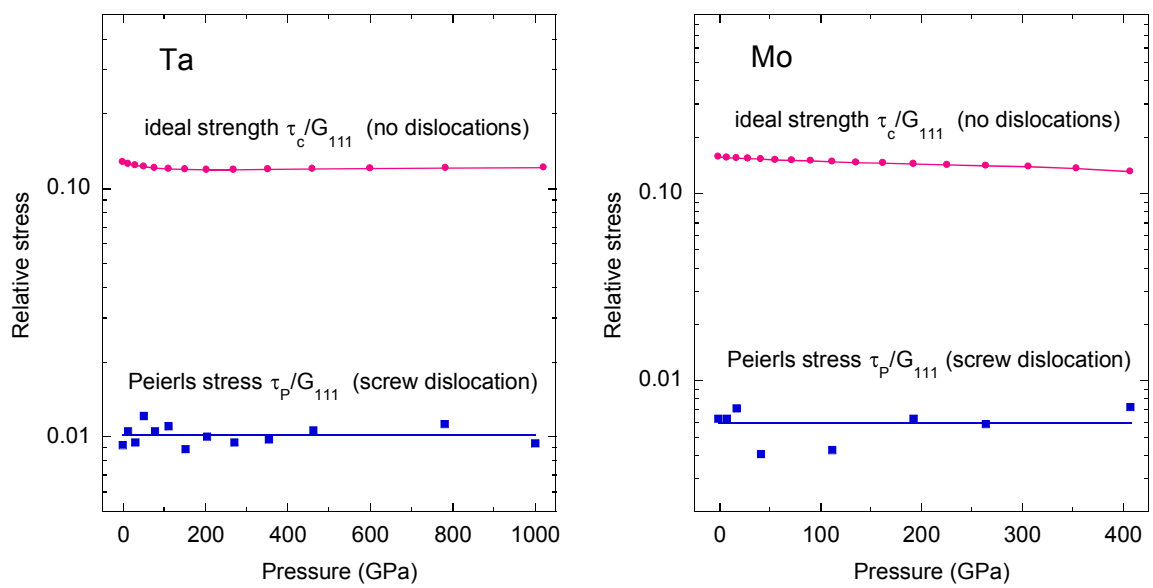

Figure 19. Pressure dependence of the scaled Peierls stress τ_P / G_{111} in Ta and Mo, as calculated from GFBC/MGPT atomistic simulations (solid square points) and compared with a constant average (solid line below). Also shown for comparison is the corresponding scaled ideal strength τ_c / G_{111} (solid circles and solid line above).

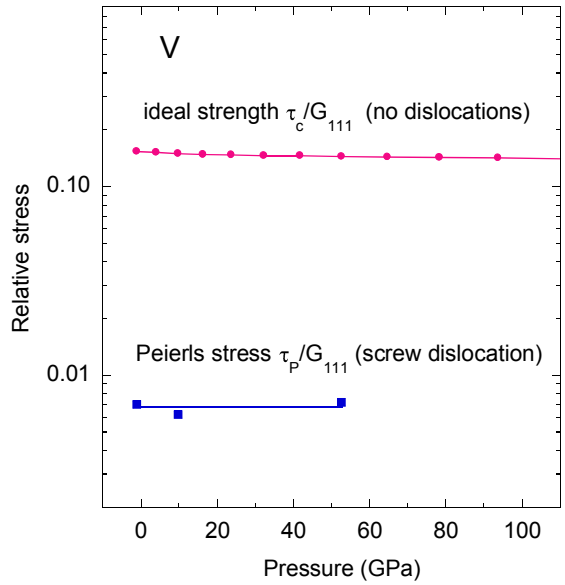

Figure 20. Pressure dependence of the scaled Peierls stress τ_P / G_{111} in V, as calculated from GFBC/MGPT atomistic simulations (solid square points) and compared with a constant average (solid line below). Also shown for comparison is the corresponding scaled ideal strength τ_c / G_{111} (solid circles and solid line above).

Fig. 19 and for V in Fig. 20. Shown for comparison in these figures are the corresponding average values of τ_P / G_{111}, which are 0.0102 in Ta, 0.0059 in Mo and 0.0068 in V. Although there are significant fluctuations from these constant values in Ta and Mo at pressures below 150 GPa, overall they are fairly representative over the entire pressure range in each case. Also shown in Figs. 19 and 20 are the corresponding values of the scaled ideal strength τ_c / G_{111}, which is more than an order of magnitude larger for each metal.

4.4 Activation enthalpy

The pressure and shear-stress dependent activation enthalpy $\Delta H(P,\tau)$ for dislocation motion provides the necessary connection between the $\tau = 0$ kink-pair formation energy E_{kp}^{f} and the high shear-stress $\tau = \tau_P$ limit where the rigid screw dislocation moves without kink formation. The calculation of $\Delta H(P,\tau)$ requires an atomistic simulation of kink formation under both pressure and shear stress, which is convenient to perform at constant atomic volume rather than constant total stress. To do so, we first consider the thermodynamic enthalpy of N simulation atoms at zero temperature, $H = N(E + P\Omega)$, and manipulate the required enthalpy change into a useful form for constant-volume calculations. In this regard, Hirth has argued [73] that at high pressure there should be an explicit contribution to the

activation enthalpy at constant pressure arising from the "$P\Omega$" term in H, but as we show below such a contribution drops out in a constant-volume formulation.

We begin in the $\tau = 0$ limit, where the change in enthalpy to form either a kinked or un-kinked screw dislocation at constant pressure P can be written

$$\Delta H(P) = N[E_2(\Omega_2) - E_1(\Omega_1) + P\Delta\Omega] \ , \tag{10}$$

with E the average energy per atom and $\Delta\Omega = \Omega_2 - \Omega_1$. Here the subscript "1" refers to the initial state and the subscript "2" to the final state. While the total volume change $N\Delta\Omega$ may be significant if N is large, the average change in atomic volume $\Delta\Omega$ is small, so that one may perform a Taylor series expansion of the term $E_2(\Omega_2)$ about the volume Ω_1:

$$\begin{aligned} E_2(\Omega_2) &= E_2(\Omega_1) + \frac{\partial E_2(\Omega_1)}{\partial\Omega}\Delta\Omega + \cdots \\ &= E_2(\Omega_1) - P\Delta\Omega + \cdots \end{aligned} \ , \tag{11}$$

To obtain the second line of Eq. (11), we have re-expanded the derivative term in the first line about Ω_2 and noted that at constant pressure

$$P = -\frac{\partial E_1(\Omega_1)}{\partial\Omega} = -\frac{\partial E_2(\Omega_2)}{\partial\Omega} \ . \tag{12}$$

Using Eq. (11) in Eq. (10), one finds that the pressure terms cancel and one is left with the result, correct to first order in $\Delta\Omega$,

$$\Delta H(P) = N\Delta E(\Omega_1) = N[E_2(\Omega_1) - E_1(\Omega_1)] \ . \tag{13}$$

The leading correction to this result is of the order $(\Delta\Omega)^2$ and negligible.

Equation (13) can be immediately connected with the two important limiting cases already considered above. First, in the formation of the rigid screw dislocation from the perfect bcc lattice, we identify $N\Delta E$ with the formation energy at constant volume E^f_{screw} in Eq. (8). Second, in the formation of an isolated pair of kinks on the screw dislocation line, we identify $N\Delta E$ with the kink-pair formation energy at constant volume E^f_{kp} in Eq. (9). In the latter case, we may generalize Eq. (13) to the case of two attractively interacting kinks separated by

a distance λ and held in (unstable) equilibrium under an applied shear stress τ to obtain the desired total activation enthalpy:

$$\Delta H(P,\tau) = E_{kp}^{f}(\Omega) + E_{\text{int}}(\lambda) - \tau(\lambda)\lambda hb \ , \tag{14}$$

where E_{kp}^{f} remains the constant-volume kink-pair formation energy at infinite separation and E_{int} is the additional interaction energy at separation λ. In the small shear stress limit $\tau < 0.2\tau_P$, the kink-kink separation λ is larger than the kink width (~ 7*b* for Ta) and $E_{\text{int}}(\lambda)$ varies as λ^{-1} and $\tau(\lambda)$ varies as $\lambda^{-1.5}$ [13], making it possible to evaluate the final two terms in Eq. (14).

For larger shear stresses $\tau > 0.2\tau_P$, a special atomistic simulation procedure has been developed to evaluate $\Delta H(P,\tau)$. In the procedure, a self-consistent 3D atomistic model of kink-pair formation and migration is constructed involving three new steps in our GFBC/MGPT simulations: First, a straight a/2<111> screw dislocation is constructed and is then fully relaxed under a trial applied shear stress. The straight screw dislocation line is lifted in energy above the valley of the Peierls potential, and the degree of lifting depends on the magnitude of the applied shear stress. Next, a 3D kink-pair model is constructed from this reference configuration. In this construction, the kink separation distance λ is treated as a fixed parameter, which is chosen to approximate the separation distance at which the kink pair is just balanced by the applied stress. Under the constraint of fixed λ, the kink pair configuration is then fully relaxed. The total energy is calculated by summing over the atom-to-atom energy difference between the relaxed 3D configuration and the straight screw dislocation under the same applied shear stress. This produces the sum of the first two terms on the right-hand side of Eq. (14). Finally, the shear stress τ for kink-pair formation at the separation λ and the work done by that stress is calculated using the trapezoid model of Koizumi *et al*. [74]. This gives the final term in Eq. (14). This approach has been successfully applied here to calculate $\Delta H(P,\tau)$ for shear stresses up to $0.9\tau_P$.

Using this procedure, we have calculated a full kink-pair activation enthalpy curve at a total of four selected pressures in Ta and three pressures each in Mo and V. Representative results for Ta and Mo are displayed in Figs. 21 and 22, respectively. In these figures we have plotted both individual points obtained from GFBC/MGPT atomistic simulations and smooth analytic fits to the results. The latter provide a means to directly input atomistic activation enthalpy data into DD plasticity and yield strength simulations and will be discussed further

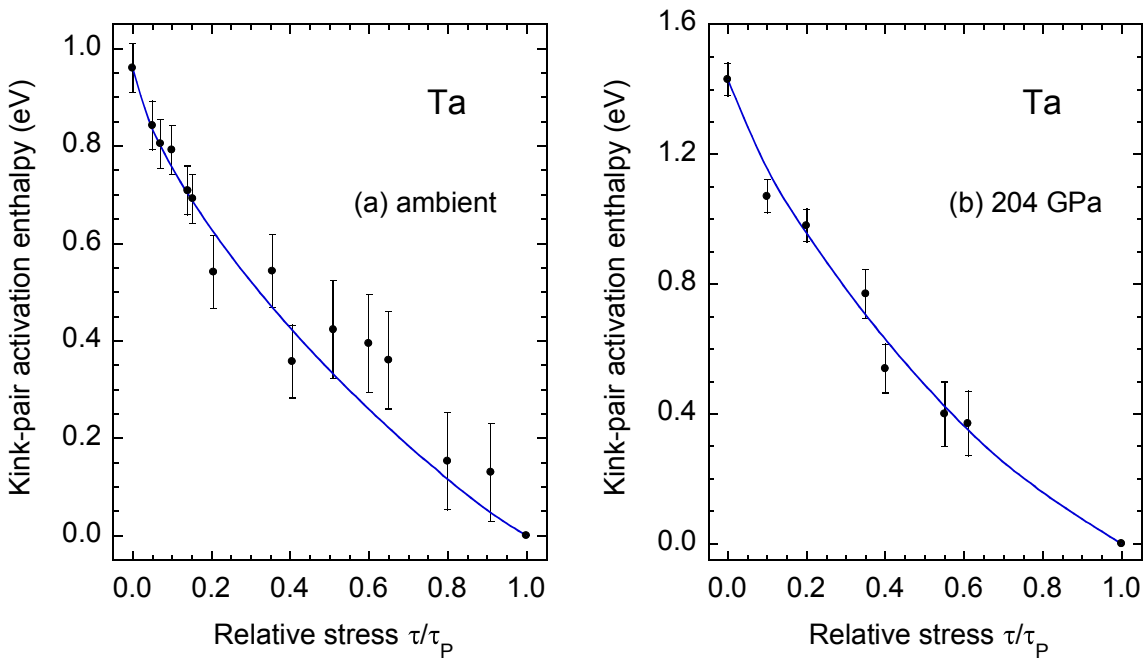

Figure 21. Activation enthalpy for Ta at two selected pressures, as calculated from GFBC/MGPT atomistic simulations (solid points) and from an analytic fit [Eq. (15)] to these data (solid lines). (a) Ambient pressure; (b) P = 204 GPa.

below in Sec. 5.2. The individual simulation points at shear stresses above $0.2\tau_P$ have significant error bars of up to 0.1 eV, but the high stress part of the curve is well constrained by the requirement that $\Delta H(P,\tau)$ vanish at $\tau = \tau_P$, so quite regular fits can be obtained.

4.5 Dislocation mobility near and above the Peierls stress

At finite temperature, a dislocation moves under the influence of thermal fluctuations and as the temperature rises the possibility of forming double kinks is increased [75]. When the applied shear stress is high and approaches τ_P, multiple kinks begin to be formed and it actually becomes possible to see them in dynamic atomistic simulations. To investigate this phenomenon in bcc transition metals, we have preformed a large scale finite-temperature MD GFBC/MGPT simulation of $a/2<111>$ screw dislocation motion in Ta under pure shear loading at a stress level about 10% below the Peierls stress. Here the simulation cell was constructed in a cylindrical geometry with periodic boundary conditions along the $<111>$ dislocation line direction. The atomistic region of the cell had a radius of 40*b* and was 200*b*

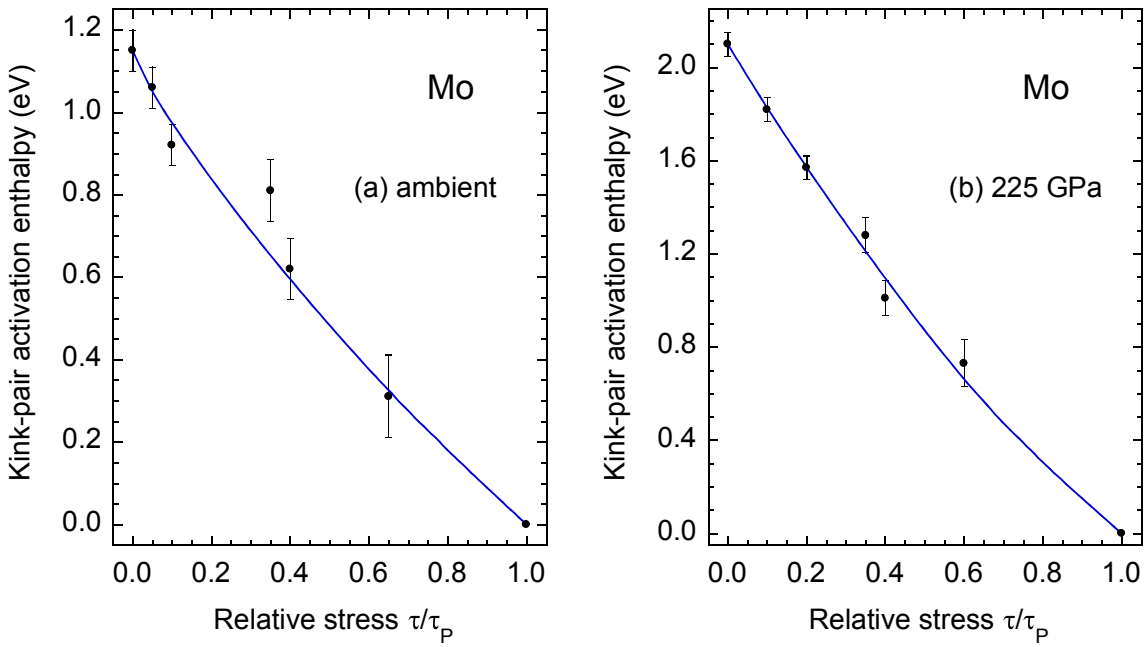

Figure 22. Activation enthalpy for Mo at two selected pressures, as calculated from GFBC/MGPT atomistic simulations (solid points) and from an analytic fit [Eq. (15)] to these data (solid lines). (a) Ambient pressure; (b) P = 225 GPa.

in length, containing over 1.3 million atoms. The simulation was performed at 300 K and ambient pressure with the shear stress applied on a $(\bar{1}10)$ plane in a $<111>$ direction. Our simulation results indeed reveal kink formation along the screw dislocation line, and a snapshot of the kink structure is displayed in Fig. 23.

For shear stresses $\tau > \tau_P$, the resistance to dislocation motion comes entirely from thermal vibrations and the screw dislocation velocity $v_s(P,T,\tau)$ becomes linear in the applied stress with a phonon-drag mobility that depends on pressure and temperature. To study dislocation motion above the Peierls stress at a given pressure and temperature, similar large scale MD GFBC/MGPT simulations have been performed in Ta as a function of applied shear stress. The cylindrical simulation cell geometry used was the same as just described above, except that the atomistic region of the cylinder was chosen to be somewhat larger with a radius of 50*b* and length of 400*b*, so that about 4 million atoms were simulated in each case. In these simulations the screw dislocation was initially placed at the center of the simulation box. The simulation cell was then pre-strained at the plastic strain corresponding to the applied shear stress τ, so that the simulation could be run at constant volume rather than constant

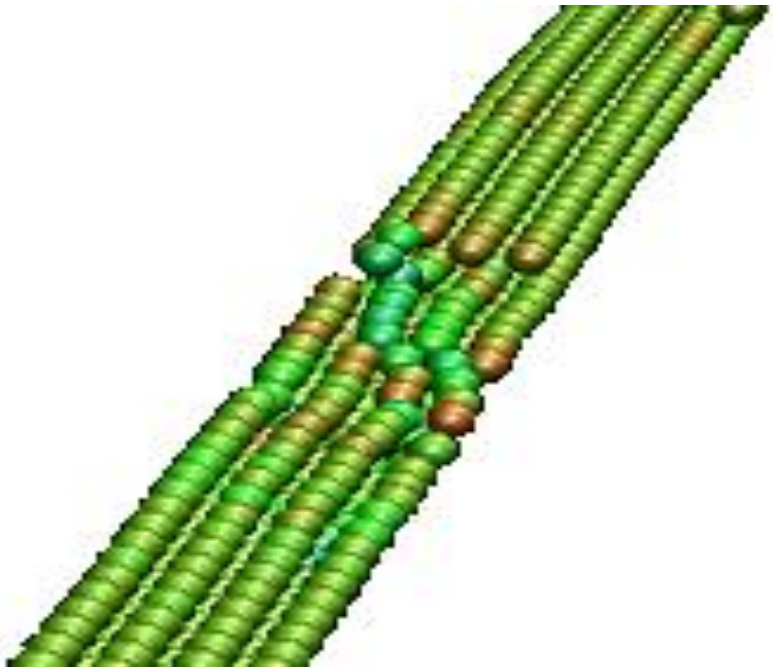

Figure 23. A snapshot of kink formation on a $<111>$ screw dislocation along the $<\bar{1}\bar{1}2>$ direction on the $(\bar{1}10)$ plane in Ta at 300 K, ambient pressure and an applied shear stress $\tau = 0.9\tau_P$, as obtained with an MD GFBC/MGPT simulation.

total stress [67]. The molecular dynamics was carried out by integrating Newton's equations of motion for the atoms in the atomistic region using a time step of 1 fs at constant temperature, which was maintained using a Nose′-Hoover thermostat [76,77]. The displacements of the atoms in the Green's function region of the simulation cell were updated every 10 MD time steps while the atoms in the continuum region were kept fixed.

Using this computational scheme, we have focused our MD GFBC/MGPT simulations on bcc Ta within the applied stress range from 1.05 τ_P to 1.25 τ_P and the pressure range from ambient to 400 GPa. Within these ranges we found that the phonon-drag mobility was approximately linear in the scaled temperature, $T/T_m(P)$, where $T_m(P)$ is the pressure-dependent melt temperature as determined from previous MGPT calculations on Ta [14]. Consequently, at each pressure treated we considered only temperatures of approximately 0.3 $T_m(P)$ and 0.6 $T_m(P)$ in our MD simulations. The actual temperature values were 900 and 1800 K at ambient pressure, 1545 and 3090 K at 50 GPa, and 2580 and 5200 K at 230 GPa. The results of these simulations for $v_s(P,T,\tau)$ are plotted in Fig. 24 together with least squared linear analytic fits to the simulation data. In these simulations the screw dislocation was found to glide on a {110} plane at all pressures, temperatures and applied stress levels

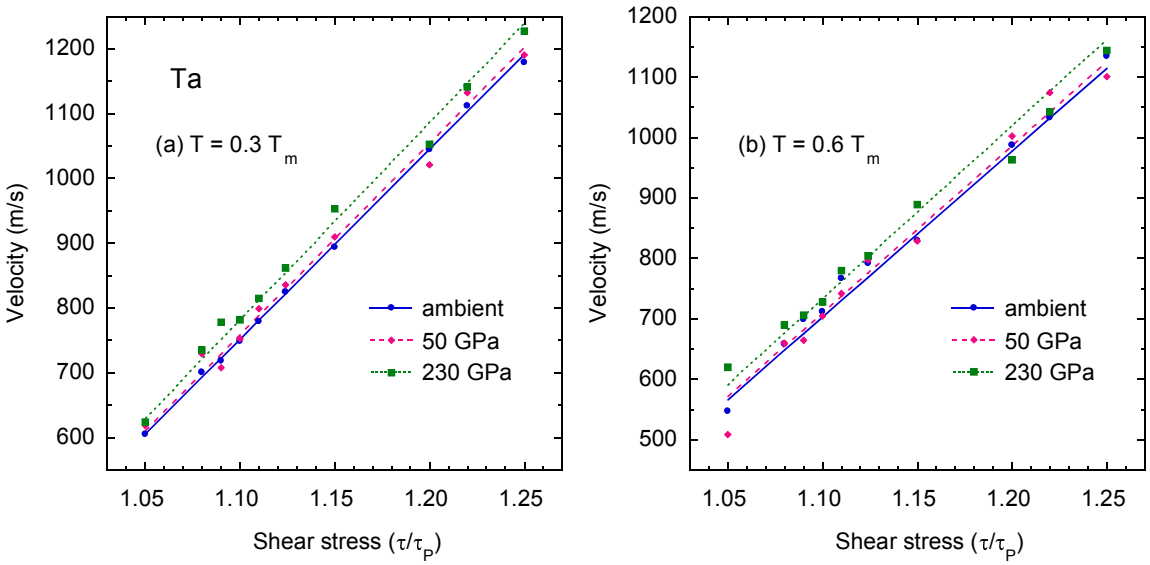

Figure 24. Screw dislocation velocity above the Peierls stress in the phonon drag regime for Ta, as calculated by MD GFBC/MGPT simulations (points) with linear analytic fits [Eqs. (18)-(20)] to the simulation data (lines). (a) Temperature 0.3 $T_m(P)$; (b) 0.6 $T_m(P)$.

considered. The analytic fits in Fig. 24 show that the velocity data is well represented by a form that is linear in the pressure P as well as in $T/T_m(P)$ and τ/τ_P. These fits will be discussed further in Sec. 5.1 below and used to provide an analytic form of the phonon-drag mobility suitable for DD simulations.

5. Multiscale Modeling of Single-Crystal Plasticity

As a practical matter, all computational dislocation dynamics methods require a robust analytic representation of the mobility of individual dislocation segments. In this section we first consider appropriate analytic forms to represent the atomistic results for $a/2<111>$ screw dislocations discussed above in Sec. 4 within both the legacy lattice-based DD code [21,22] and the modern node-based ParaDiS code [27-30]. Using these analytic functions, we then discuss atomistically informed DD simulations of yield stress and plasticity for Ta and Mo as a function of pressure, temperature and strain rate to complete our multiscale modeling of these materials.

5.1 Analytic representations of dislocation velocity

As shown in Fig. 21 for Ta and Fig. 22 for Mo, the activation enthalpy for $a/2<111>$ screw dislocation motion below the Peierls stress in the thermally activated regime is accurately represented by following well known analytic form:

$$\Delta H(P,\tau) = \Delta H_0(P)\left[1-\left(\frac{\tau}{\tau_P}\right)^p\right]^q \quad , \tag{15}$$

where here $\Delta H_0(P)$ and τ_P are calculated atomistic quantities and p and q are additional parameters that have been determined by a least-squares fit to the atomistic simulation data for $\Delta H(P,\tau)$. As can be inferred from Eq. (14), $\Delta H_0(P)$ is just the kink-pair formation energy at $\tau = 0$:

$$\Delta H_0(P) = E_{kp}^f(\Omega)\Big|_{P=P_0(\Omega)} \quad . \tag{16}$$

Values of the parameters $\Delta H_0(P)$, τ_P, p and q are listed in Table 4 for the ten cases for which full activation enthalpy curves for Ta, Mo and V have been calculated.

Equation (15) is used in both the lattice-based and ParaDiS DD codes although with different treatments of the internal parameters $\Delta H_0(P)$, τ_P, p and q. In the lattice-based code, the parameters in Table 4 have been used directly, except for τ_P in Ta, which has been scaled by a factor of 0.5 to account for the apparent overestimate of the Peierls stress relative to experiment noted in Fig. 18. In ParaDiS, however, additional modeling has been introduced

Table 4. Calculated ($\Delta H_0, \tau_P$) and fitted (p, q) parameters entering the activation enthalpy $\Delta H(P,\tau)$ of Ta, Mo and V, as represented by Eq. (15).

Metal	P (GPa)	ΔH_0 (eV)	p	q	τ_P (GPa)
Ta:					
	ambient	0.96	0.71	1.10	0.577
	51	1.22	0.85	1.34	1.283
	204	1.43	0.81	1.27	2.158
	354	1.89	0.84	1.31	3.139
Mo:					
	ambient	1.15	0.84	1.06	0.860
	55	1.69	0.93	1.14	1.349
	225	2.10	0.97	1.23	2.035
V:					
	ambient	0.68	0.74	1.12	0.360
	9.7	0.90	0.78	1.10	0.369
	53	1.06	0.82	1.14	0.633

to smooth the pressure dependence of the internal parameters. First, p and q are assumed to be universal constants, which have been fixed in our ParaDiS simulations at p = 0.50 and q = 1.23. In addition, $\Delta H_0(P)$ and τ_P are assumed to obey the high pressure scaling laws

$$\Delta H_0(P) = a_0 G_{111}(P)[b(P)]^3 \tag{17}$$

and

$$\tau_P = b_0 G_{111}(P) \ , \tag{18}$$

where the constants a_0 and b_0 are determined at ambient pressure from our atomistic results, with the caveat that τ_P in Ta is again scaled by a factor of 0.5. Specifically, we have taken a_0 to be 0.11 eV/GPa-Å^3 in Ta and 0.066 eV/GPa-Å^3 in Mo, and b_0 to be 0.0051 in Ta and 0.0062 in Mo.

In the lattice-based DD code, the screw dislocation velocity below the Peierls stress in the thermally activated regime is calculated as

$$v_s(P,T,\tau) = v_0(P)\exp\left[-\frac{\Delta H(P,\tau)}{k_B T}\right] , \tag{19}$$

where $v_0(P)$ is a constant velocity computed in terms of the pressure-dependent Debye frequency and burgers vector of the bcc lattice and the length of the screw dislocation [21]. In this case, dislocation motion above the Peierls stress is not treated explicitly, so for $\tau > \tau_P$ one takes $v_s = v_0$.

In the ParaDiS code, on the other hand, a modified form of Eq. (19) is used in the thermal activation regime, as described below, and above the Peierls stress in the phonon drag regime, the screw dislocation velocity is modeled by the linear equations used to fit the Ta data in Fig. 24, which have the form

$$v_s(P,T,\tau) = M_s(P,T)\left(A\frac{\tau}{\tau_P} - B \right) , \tag{20}$$

where

$$M_s(P,T) = C_0(1 - C\frac{T}{T_m} + DP) \ . \tag{21}$$

Here C_0 is the shear sound speed at ambient pressure and *A*, *B*, *C* and *D* are constants determined by the least-squares fit to the Ta data. The latter have values *A* = 1.525, *B* = 1.28625, *C* = 0.20323 and *D* = 1.627 × 10^{-4} GPa^{-1}, and here these values have been used for both the Ta and Mo DD simulations with ParaDiS discussed in Sec. 5.2. Regarding the material dependent shear sound speed, in Ta we have used C_0 = 2048 m/s and in Mo we have used C_0 = 3496 m/s.

The modified form of Eq (19) used in ParaDiS for the screw dislocation velocity in the thermally activated regime below τ_P is of the form

$$v_s(P,T,\tau) = M_s(P,T)(A - \beta B)\frac{\tau}{\tau_P}\exp\left[-\frac{\Delta H(P,\tau)}{k_B T} \right] , \tag{22}$$

where the pre-exponential terms have been chosen to provide approximate continuity of v_s and its first stress derivative across the Peierls stress τ_P with Eq. (20) for the phonon-drag contribution. The choice β = 1 in Eq. (22) gives continuity of v_s at $\tau = \tau_P$, but a discontinuity in the first derivative. However, by matching Eqs. (20) and (22) at a shear

stress τ slightly below τ_P, one can maintain continuity of both v_s and its first derivative for a value of β near 1.

In addition to a velocity function for the screw dislocations, a velocity function for the edge dislocations is also required in the DD codes. Here simplifying assumptions are made without any specific guidance from atomistic calculations [21,22,27-30]. In the lattice-based DD code, these functions are used directly for the screw and edge dislocation segments. In ParaDiS, after the basic segment velocity functions are established, the code utilizes the screw and edge segment mobilities to obtain a general velocity at each dislocation node by mixing the two mobility functions. The details of this mixing and the resulting nodal velocity are given in detail in Ref. 30.

5.2 Temperature- and pressure-dependent plastic flow

Using the ParaDiS simulation code and the above described velocity functions, we have carried out DD simulations in Ta and Mo for a range of pressure and temperature conditions. In the case of Ta, we have also carried out the simulations at different strain rates, as well as simulations with the lattice-based DD code over a wider range of pressures. The simulations focus on the initial yield behavior rather than later stage strain hardening. The ParaDiS simulations start with an initial dislocation configuration consisting of screw lines with the total density of $5\times10^{12}/m^2$ in a cubic 5 μm simulation box with periodic boundary conditions along all directions. The simulations are carried out under a constant strain rate. The flow stress response is initially elastic until dislocations start to move. When the plastic strain rate reaches the applied strain rate, the flow stress shows a steady state behavior, as shown in the stress-strain response curves. The yield stress is thus obtained at the end of the simulations when the flow stress reaches a nearly steady value. The loading is uniaxial tension and the orientation is along [123]. Under this single slip orientation, the Schmid factor is 0.467. The resolved yield stress is obtained from the flow stress multiplied by the Schmid factor.

The simulated ParaDiS stress-strain curves for Ta are shown in Fig. 25 at ambient pressure and at 30 GPa, for temperatures of 300, 600 and 1000 K, and at strain rates of 1/s and 1000/s. All simulated responses show an initial elastic behavior, then plastic deformation when the flow stress is high enough to move the dislocations. The dislocation densities also go through orders of magnitude increase in these simulations. The corresponding resolved yield stress values obtained are shown in Fig. 26. The resolved yield stresses clearly show a strong dependence on strain rate, pressure and temperature. The higher the strain rate, the higher the

pressure and the lower the temperature, the higher the yield stress. This is expected for plastic deformation process dominated by thermally activated dislocation motion. The pressure dependence comes from the fact that both the activation enthalpy and the Peierls stress are higher at higher pressures. The temperature dependence is direct through the dislocation velocity functions, Eqs. (20) and (22). As for the strain rate dependence, higher stress is required to move the dislocations with a higher deformation rate. The dislocations multiply faster and also move faster at higher strain rate. The simulations show that the dislocation density at yield for the higher strain rate is about 25 times the density at the lower strain rate. This means the main effect responding to the high strain rate is through the velocity speed up rather than density multiplication alone.

In the case of Ta, calculations of the temperature dependence of the yield stress have also been performed over a wider pressure range using the lattice-based DD code. These results are plotted in Fig. 27 and cover pressures as high as 204 GPa. These simulations were performed at a quasi-static strain rate of 10^{-3}/s, which for ambient pressure allows a close

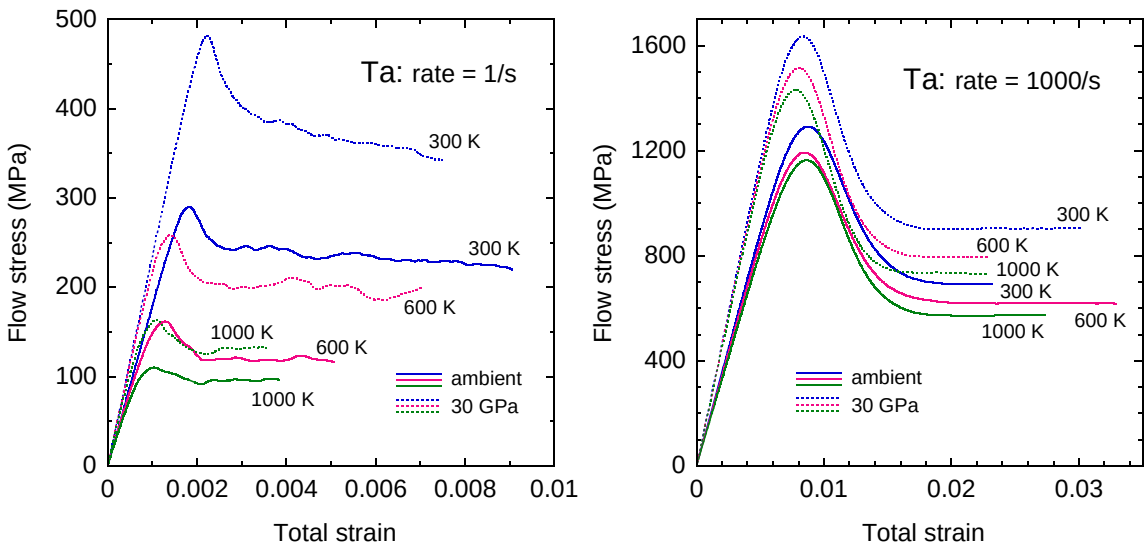

Figure 25. Simulated stress-strain curves of single-crystal Ta, as obtained with the ParaDiS DD code. The left panel shows the results at a strain rate of 1/s; and the right panel results at a strain rate of 1000/s. For each strain rate, the simulations were performed at two pressures values, ambient and 30 GPa and for temperatures of 300, 600 and 1000 K. The nearly steady state flow stress values at the end of the simulations are used to obtain the resolved yield stress values in Fig. 26.

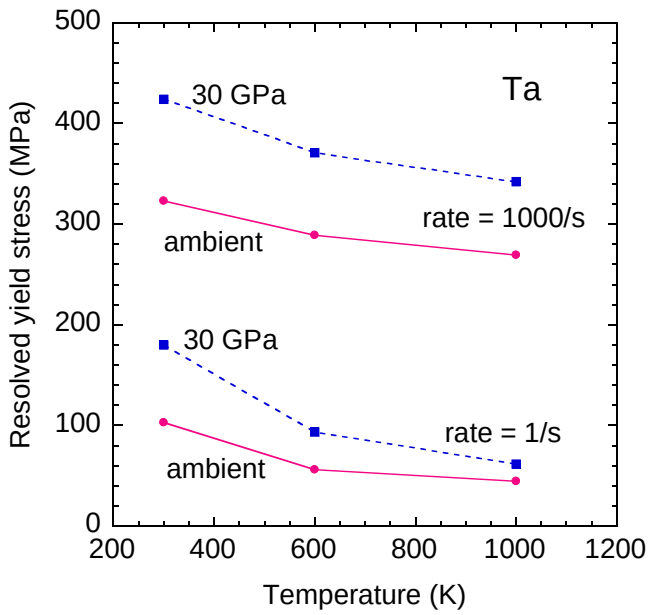

Figure 26. The resolved yield stress values for single-crystal Ta corresponding to the stress-strain curves in Fig. 25. The solid square symbols are values at 30 GPa, and the solid circles values at ambient pressure. The upper curves are results obtained at a strain rate of 1000/s, while the lower curves were obtained at 1/s.

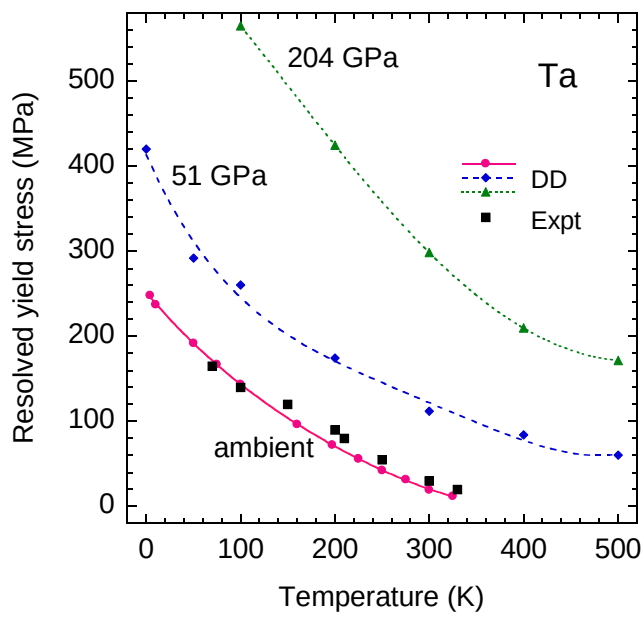

Figure 27. Temperature dependence of the resolved yield stress at three pressures in single-crystal Ta, as obtained using the legacy lattice-based DD code at a quasi-static strain rate of 10^{-3}/s. Experimental data at ambient pressure and the same strain rate (solid squares) are from Ref. 78.

comparison with accurate experimental data [78]. While our factor of two scaling down of the Peierls stress was motivated in part by a desire to normalize to experiment at one point on the ambient pressure curve, the full temperature dependence of the experimental data is nonetheless well captured by our simulation. Using ParaDiS, we performed verification simulations at ambient pressure using the same parameters and loading conditions and obtained reasonable consistency when compared with the results obtained using the lattice based DD code.

We have also carried out ParaDiS simulations for single-crystal Mo at ambient pressure for temperatures of 300, 600 and 1000 K and at 225 GPa for temperatures of 600 and 1000 K. These simulations were all carried out at a strain rate of 1/s and the simulated stress-strain curves are shown in Fig. 28. An attempt to simulate the additional point at 225 GPa and 300 K was made, but due to the extremely large activation enthalpy and low temperature, the DD time-step required was too small to obtain meaningful results. We have, however, estimated the resolved yield stress for this point in the following manner. Using the rate equation,

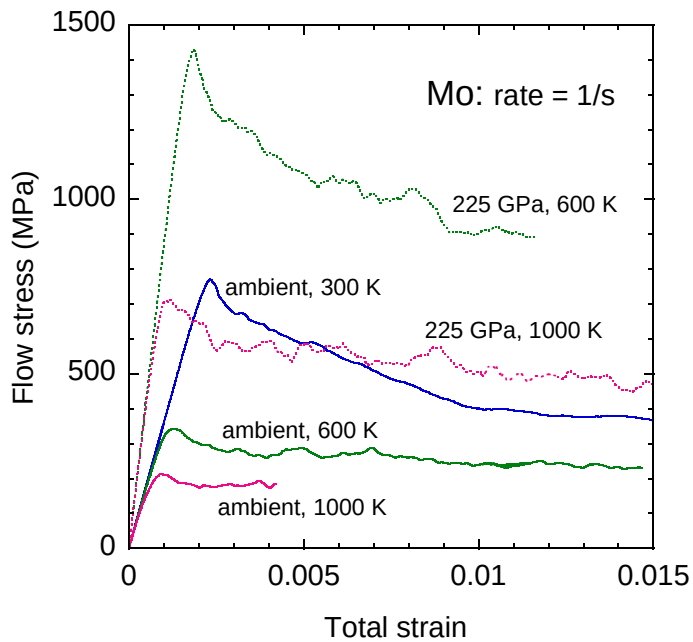

Figure 28. Simulated stress-strain curves for single-crystal Mo at a strain rate of 1/s, as obtained with the ParaDiS DD code. The solid lines are results obtained at ambient pressure for temperatures of 300, 600 and 1000 K. The dashed lines are results obtained at 225 GPa for temperatures of 600 and 1000 K. As in the case of Ta, the nearly steady state flow stress values at the end of the simulations were used to obtain the resolved yield stresses plotted in Fig. 29.

$\dot{\varepsilon} = \rho b v_s$ = constant, we first used the simulated dislocation density ρ at 225 GPa and 600 K to estimate its value at 300 K. Then combining this rate equation and the velocity function in Eq. (22) we obtained an estimate of the resolved yield stress. This value together with the resolved yield stresses obtained directly from the stress-strain curves in Fig. 28 are shown in Fig. 29. Again, one sees a strong dependence on pressure and temperature in these results. For comparison we also show in Fig. 29 ambient pressure and temperature experimental data for the resolved yield stress in Mo from the Seeger group in Germany [70,71] and from the Aono group in Japan [79]. We note, however, that this data was measured at quasi-static strain rates as opposed to the 1/s strain rate in our simulations. Since the resolved shear stress value is expected to decrease with decreasing strain rate, the data should be lower in magnitude than the simulation, which they are. However, the two experimental data points themselves have a rather large discrepancy. This shows the sensitivity of the experimental measurement to sample conditions.

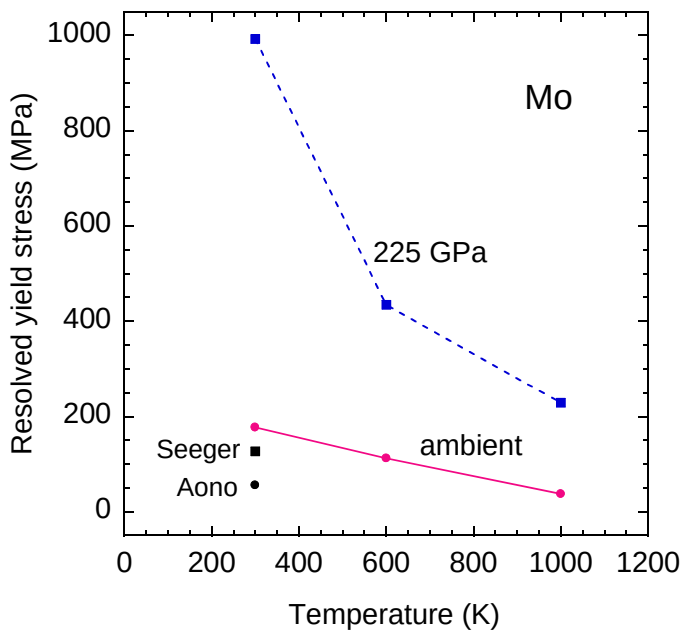

Figure 29. Resolved yield stresses of single crystal Mo obtained at ambient pressure (solid circles and solid lines) and at 225 GPa (solid squares and solid lines). Except for the estimated point at 225 GPa and 300 K (see text), the remaining results were obtained from the stress-strain curves in Fig. 28 obtained at a strain rate of 1/s. For comparison ambient temperature and pressure experimental data points from the Seeger group [70,71] and the Aono group [79] at lower quasi-static strain rates are also shown.

6. Summary and Conclusions

In this paper we have successfully combined first-principles PP and FP-LMTO electronic calculations, quantum-based GFBC/MGPT atomistic simulations, and atomistically informed lattice-based and ParaDiS dislocation dynamics simulations at the microscale to study the fundamental properties of $a/2<111>$ screw dislocations and the plasticity that they drive in the bcc transition metals Ta, Mo and V over a wide range of pressure. Within this information passing approach to the multiscale modeling of mechanical properties, the electronic structure calculations have allowed us to accurately calculate the *material specific* high-pressure elasticity and range of bcc mechanical stability in these metals, and to provide fundamental bcc data on the equation of state, ideal strength and γ surfaces needed to validate multi-ion MGPT interatomic potentials. In particular, we have shown that the present MGPT potentials for Ta and Mo predict very accurately the {110} and {211} γ surfaces relevant to screw dislocation structure and motion over pressures ranging from ambient to 400 GPa. With the GFBC/MGPT atomistic simulations, we have studied in detail the pressure-dependent properties of the $a/2<111>$ screw dislocations, including the core structure and energy, the Peirels stress τ_P and its orientation dependence, the kink-pair formation energy E_{kp}^f and the activation enthalpy $\Delta H(P,\tau)$ for dislocation motion below τ_P, and the dislocation velocity $v_s(P,T,\tau)$ in the phonon drag regime above τ_P. These properties exhibit a complex blend of both material specific and generic scalable behavior. The core structure is materials specific and varies qualitatively with material and pressure, while the Peierls stress τ_P is always minimized for <111> shear stresses on {110} slip planes and scales reasonable well with the G_{111} shear modulus to 1000 GPa in Ta, 400 GPa in Mo and 53 GPa in V. The kink pair formation energy E_{kp}^f is less robust in its scaling properties but varies approximately as $G_{111}b^3$ at high pressure. The activation enthalpy $\Delta H(P,\tau)$ and phonon-drag velocity $v_s(P,T,\tau)$ lend themselves to analytic fits as a function of pressure, temperature and shear stress that can be used directly in the DD simulations to quantify the motion of individual dislocation segments. Using these analytic functions, we have successfully performed predictive lattice-based and ParaDis simulations of flow stress and resolved yield stress in Ta and Mo as a function of pressure, temperature and strain rate.

Acknowledgements

This work was performed under the auspices of the U. S. Department of Energy by the Lawrence Livermore National Laboratory in part under Contract W-7405-Eng-48 and in part under Contract DE-AC52-07NA27344. We would like to thank A. Arsenlis, R. Becker, G. Hommes, and M. Rhee for helpful discussions related to the ParaDiS simulations.

References

[1] S. Yip, ed., Modeling Industrial Materials: Connecting Atomistic and Continuum Length Scales, special issue of J. of Computer-Aided Mater. Design, Vol. 3**,** Nos. 1-3 (1996).

[2] H. M. Zbib, J. P. Hirth, T. Khraishi and R. Thomson, eds., Multi-Scale Modeling of Deformation and Fracture, special issue of J. of Engineering Mater. and Technology, Vol. 121**,** No. 2 (1999).

[3] V. V. Bulatov, T. Diaz de la Rubia, R. Phillips, E. Kaxiaras and N. Ghoniem, eds., Multiscale Modelling of Materials, MRS Symposium Proceedings Volume 538 (Materials Research Society, Warrendale, 1999).

[4] L. Levine, L. Kubin and R. Becker, eds., Dislocations 2000: An International Conference on the Fundamentals of Plastic Deformation, special issue of Mater. Sci. and Engineering A, Vols. 309-310 (2001).

[5] E. A. Chandler and T. Diaz de la Rubia, eds., Bodega Bay International Workshop on Multiscale Modeling of Material Strength and Failure, special issue of J. of Computer-Aided Mater. Design, Vol. 9, No. 2 (2002).

[6] B. Devincre, D. Rodney and P. Veyssiere, eds., Dislocations 2004, special issue of Mater. Sci. and Engineering A, Vols. 400-401 (2005).

[7] Z. Xiao Guo, ed., Multiscale Materials Modeling (Woodhead Publishing, Abington, 2007).

[8] P. Gumbsch, ed., 3rd International Conference on Multiscale Materials Modelling, MMM 2006, J. of Computer-Aided Mater. Design, Vol. 14, Supplement 1 (2007).

[9] W. Xu and J. A. Moriarty, Phys. Rev. B, 54 (1996) 6941 and Comput. Mater. Sci., 9 (1998) 348.

[10] S. Ismail-Beigi and T. A. Arias., Phys. Rev. Lett., 84 (2000) 1499.

[11] C. Woodward and S. I. Rao, Philos. Mag., A81 (2001) 1305.

[12] S. I. Rao and C. Woodward, C., Philos. Mag., A81 (2001) 1317.

[13] L. H. Yang, P. Söderlind and J. A. Moriarty, Philos. Mag. A, 81 (2001) 1355.

[14] J. A. Moriarty, J. F. Belak, R. E. Rudd, P. Söderlind, F. H. Streitz and L. H. Yang, J. Phys.: Condens. Matter, 14 (2002) 2825 and references therein.

[15] C. Woodward and S. I. Rao, Phys. Rev. Lett. 88 (2002) 21642.

[16] J. A. Moriarty, V. Vitek, V. V. Bulatov and S. Yip, J. of Computer-Aided Mater. Design, 9 (2002) 99 and references therein.

[17] S. L. Frederiksen and K. W. Jacobsen, Philos. Mag., 83 (2003) 365.

[18] M. Mrovec, D. Nguyen-Manh, D. G. Pettifor and V. Vitek, Phys. Rev. B, 69 (2004) 94115.

[19] J. A. Moriarty, L. X. Benedict, J. N. Glosli, F. H. Streitz, M. Tang and L. H. Yang, J. Mater. Res., 21 (2006) 563 and references therein.

[20] L. Kubin, G. Canova, M. Condat, B. Devincre, V. Pointikis and Y. Brechet, Solid State Phenomena, 23-24 (1992), 455.

[21] M. Tang, L. P. Kubin and G. R. Canova, Acta Mater., 46 (1998) 3221.

[22] M. Tang, in: Handbook of Materials Modeling, Vol. 1, ed. S. Yip (Springer, Amsterdam, 2005), p. 827.

[23] M. Rhee, H. Zbib, H. Huang and T. Diaz de la Rubia, Modelling Simul. Mater. Sci. Eng., 6 (1998) 467.

[24] K. Schwarz, J. Appl. Phys., 85 (1999) 108.

[25] N. Ghoniem and L. Sun, Phys. Rev. B, 60 (1999) 128.

[26] D. Weygand, L. Friedman, E. Van der Giessen and A. Needleman, Modelling Simul. Mater. Sci. Eng., 10 (2002) 437.

[27] V. V. Bulatov and W. Cai, Computer Simulations of Dislocations (Oxford Press, Oxford, 2006).

[28] V. V. Bulatov, L. L. Hsiung, M. Tang, A. Arsenlis, M. C. Bartelt, W. Cai, J. N. Florando, M. Hiratani, M. Rhee, G. Honnes, T. G. Pierce and T. Diaz de la Rubia, Nature, 440 (2006) 1174.

[29] W. Cai, A. Arsenlis, C. Weinberger and V. Bulatov, J. Mech. Phys. Solids, 54 (2006) 561.

[30] A. Arsenlis, W. Cai, M. Tang, M. Rhee, T. Oppelstrup, G. Hommes, T. G. Pierce and V. V. Bulatov, Modelling Simul. Mater. Sci. Eng., 15 (2007) 553.

[31] M. Tang, G. Xu, W. Cai and V. Bulatov, Simul. Mater. Sci. and Eng., 14 (2006) 1139.

[32] M. S. Duesbery and V. Vitek, Acta Mater., 46 (1998) 1481.

[33] V. Vitek, Crystal Lattice Defects, 5 (1974) 1.

[34] M. S. Duesbery, Acta Metall., 31 (1983), 1747 and 1759.

[35] M. S. Duesbery, Proc. R. Soc. Lond. *A*, 392 (1984) 145 and 175.

[36] M. S. Duesbery, in: Dislocations in Solids, ed. F. R. N. Nabarro (Elsevier, Amsterdam, 1989), p. 67.

[37] P. Söderlind and J. A. Moriarty, Phys. Rev. B, 57 (1998) 10340.

[38] P. Söderlind, R. Ahuja, O. Eriksson, B. Johansson and J. M. Wills, Phys. Rev. B, 49 (1994) 9365.

[39] N. E. Christensen, A. L. Ruoff and C. O. Rodriguez, Phys. Rev. B, 52 (1995) 9121.

[40] Y. Ding, R. Ahuja, J. Shu, P. Chow, W. Luo and H.-K. Mao, Phys. Rev Lett., 98 (2007) 85502.

[41] B. Lee, R. E. Rudd, J. E. Klepeis, P. Söderlind and A. Landa, Phys. Rev. B, 75 (2007) 180101.

[42] P. Hohenberg and W. Kohn, Phys. Rev., 136 (1964) B864.

[43] W. Kohn and L. Sham, Phys. Rev., 140 (1965) A1133.

[44] R. M. Martin, Electronic Structure: Basic Theory and Practical Methods (Cambridge Press, Cambridge, 2004) and references therein.

[45] P. Söderlind, L. Yang, J. A. Moriarty and J. M. Wills, Phys. Rev. B, 61 (2000) 2579.

[46] L. Yang, in: Industrial Strength Parallel Computing, ed. A. Koniges (Morgan Kaufmann, San Francisco, 2000), p. 297.

[47] A. Landa, J. Klepeis, P. Söderlind, I. Naumov, O. Velikokhatnyi, L. Vitos and A. Ruban, J. Phys. Chem. Solids, 67 (2006) 2056.

[48] N. Troullier and J. L. Martins, Phys. Rev. B, 43 (1991) 1993.

[49] J. A. Moriarty, Phys. Rev. B, 38 (1988) 3199.

[50] J. A. Moriarty, Phys. Rev. B, 42 (1990) 1609 and 49 (1994) 12431.

[51] S. Rao, C. Hernandez, J. Simmons, T. Parthasarathy and C. Woodward, Philos. Mag., A77 **(**1998) 231.

[52] S. Rao, T. A. Parthasarathy and C. Woodward, Philos. Mag., A79 (1999) 1167.

[53] J. A. Moriarty, J. N. Glosli, R. Q. Hood, J. E. Klepeis, D. A. Orlikowski, P. Söderlind and L. H. Yang, in TMS 2008 Annual Meeting Supplemental Proceedings Volume I: Materials Processing and Properties (TMS, Warrendale, PA, 2008), p. 313.

[54] H. Cynn and C.-S. Yoo, Phys. Rev. B, 59 (1999) 8526.

[55] K. W. Katahara, M. H. Manghnani and E. S. Fisher, J. Phys. F: Metal Phys., 9 (1979) 773.

[56] D. L. Farber, M. Krisch, D. Antonangeli, A. Beraud, J. Badro, F. Occelli and D. Orlikowski, Phys. Rev. Lett., 96 (2006) 115502.

[57] J. Sinclair, P. Gehlen, R. Hoagland and J. Hirth, J. Appl. Phys., 49 (1978) 3890.

[58] A. N. Stroh, Phil. Mag., 3 (1958) 625 and J. Math. Phys., 41 (1962) 77.

[59] P. H. Dederichs and G. Leibfried, Phys. Rev., 188 (1969) 1175.

[60] D. C. Wallace, Thermodynamics of Crystals (Wiley, New York, 1972). Our present elastic moduli C_{ij} are the stress-strain coefficients B_{ij} defined by Wallace.

[61] A. T. Paxton, P. Gumbsch and M. Methfessel, Phil. Mag. Lett., 63 (1991) 267.

[62] J. W. Morris, Jr., C. R. Krenn, D. Roundy and M. L. Cohen, in Phase Transformations and Evolution in Materials, eds. P. E. Turchi and A. Gonis (TMS, Warrendale, PA, 2000), p. 187.

[63] P. B. Hirsch, in: Proceedings of the Fifth International Conference on Crystallography (Cambridge Press, Cambridge, 1960).

[64] M. S. Duesbery, V. Vitek and D. Bowen, Proc. R. Soc. A, 332 (1973) 85.
[65] A. Seeger and C. Würthrich, Nuovo Cim. B, 33 (1976) 38.
[66] B. Sadigh, W. Cai and V. Bulatov (2002, private communication and unpublished).
[67] M. S. Duesbery (1999, private communication and unpublished).
[68] K. Ito and V. Vitek, Phil. Mag. A, 81 (2001) 1387.
[69] S. Takeuchi, E. Kuramoto and T. Suzuki, Acta Metall. 20 (1972) 909.
[70] A. Seeger and L. Hollang, Mater. Trans. JIM, 41 (2000) 141.
[71] L. Hollang, M. Hommel and A. Seeger, Phys. Status Solidi A, 160 (1997) 329.
[72] T. Suzuki, Y. Kaminura and H. O. K. Kirchnner, Philos. Mag. A, 79 (1999) 1629.
[73] J. P. Hirth, in: Handbook of Materials Modeling, Vol. 1, ed. S. Yip (Springer, Amsterdam, 2005), p. 2879.
[74] H. Koizumi, H. O. K. Kirchner, and T. Suzuki, Philos. Mag. A, 69 (1994) 805.
[75] J. P. Hirth and J. Lothe, Theory of Dislocations (Wiley-Interscience, New York, 1982).
[76] S. Nose′, Molec. Phys., 52 (1984) 255.
[77] W. G. Hoover, Phys. Rev. A, 31 (1985) 1695.
[78] W. Wasserbach, Philos. Mag. A, 53 (1986) 335.
[79] Y. Aono, E. Kuramoto, K. Kitajima, in: Strength of Metals and Alloys, Vol. 1, ed. R. C. Gifkins (Pergamon Press, Oxford, 1982), p. 9.